



# The impact of ground-based glaciogenic seeding on clouds and precipitation over mountains: A multi-sensor case study of shallow precipitating orographic cumuli

Binod Pokharel<sup>a,\*</sup>, Bart Geerts<sup>a</sup>, Xiaoqin Jing<sup>a</sup>, Katja Friedrich<sup>b</sup>, Joshua Aikins<sup>b</sup>, Daniel Breed<sup>c</sup>, Roy Rasmussen<sup>c</sup>, Arlen Huggins<sup>d</sup>

<sup>a</sup> Department of Atmospheric Science, University of Wyoming, Laramie, WY 82071, USA

<sup>b</sup> Department of Atmospheric and Oceanic Sciences, University of Colorado, Boulder, CO 80309, USA

<sup>c</sup> Research Application Laboratory, National Center for Atmospheric Research, Boulder, CO 80307, USA

<sup>d</sup> Desert Research Institute, Reno, NV 89512, USA

## ARTICLE INFO

### Article history:

Received 24 February 2014

Received in revised form 15 May 2014

Accepted 16 May 2014

Available online 25 May 2014

### Keywords:

Glaciogenic seeding

Orographic cloud and precipitation

Radar reflectivity profiles

Airborne measurements

## ABSTRACT

This paper examines reflectivity data from three different radar systems, as well as airborne and ground-based in situ particle imaging data, to study the impact of ground-based glaciogenic seeding on shallow, lightly precipitating orographic cumuli, observed on 13 February 2012, as part of the AgI Seeding Cloud Impact Investigation (ASCII) experiment in Wyoming. Three silver iodide (AgI) generators were used, located on the windward slopes of the target mountain. This case was chosen for several reasons: the AgI generators were near the lifting condensation level, where the temperature was about  $-6\text{ }^{\circ}\text{C}$ ; cloud droplets were present in the cumulus clouds, which were rooted in the boundary layer; and the airflow, although weak, ascended over the mountain. The target mountain pass site was almost certainly impacted by seeding, according to a trace element analysis of the falling snow.

Data from three radar systems were used in the analysis of the impact of seeding on precipitation: the airborne W-band (3 mm wavelength) profiling Wyoming Cloud Radar (WCR), two Ka-band (1.2 cm) profiling Micro-Rain Radars (MRR), and a X-band (3 cm) scanning Doppler-on-Wheels (DOW) radar. The WCR was onboard a research aircraft flying geographically fixed tracks, the DOW and one MRR were located at the target mountain pass, and another MRR was upstream of the AgI generators. Composite data from the three radar systems, each with their own target and upwind control regions, indicate that the observed changes in reflectivity profiles can be explained largely by the natural emergence of shallow cumuli. A comparison with lateral control regions (i.e., over the mountain, but to the side of the AgI plumes) suggests that seeding may have further enhanced snowfall, but the signal is weak.

Particle probes at flight level and at the mountain pass site show that the concentration of small ice crystals ( $<1\text{ mm}$ ) was significantly larger downwind of the AgI generators during seeding. This too is consistent with the emergence of shallow convection, but a comparison between flight sections downwind of the AgI point sources and those to the side suggests that glaciogenic seeding increased the concentration of ice crystals of all sizes in the shallow convection.

© 2014 Elsevier B.V. All rights reserved.

**Abbreviations:** ZIP, reflectivity impact factor:  $\text{ZIP} = \Delta\text{dBZ}_T - \Delta\text{dBZ}_U$  where  $\Delta\text{dBZ} = \text{dBZ}_S - \text{dBZ}_N$ , and subscript S (N) refers to SEED (NOSEED), while subscript T (U) refers to treated or target (untreated or control); PIF, precipitation impact factor; ASCII, AgI Seeding Cloud Impact Investigation; UWKA, University of Wyoming King Air; WCR, Wyoming Cloud Radar; WCL, Wyoming Cloud Lidar; MRR, Micro-Rain Radar; DOW, Doppler on Wheels.

\* Corresponding author.

E-mail address: [bpokhare@uwyo.edu](mailto:bpokhare@uwyo.edu) (B. Pokharel).

## 1. Introduction

Ice nuclei (IN) in the atmosphere are particles that can catalyze the freezing of supercooled cloud droplets, producing ice crystals that would not otherwise form (Creamean et al., 2013). IN are naturally scarce above  $-20^{\circ}\text{C}$ , thus more snow could grow in supercooled water clouds if IN were added to such clouds. This process is important to the climate system as it links precipitation to mineral and biological aerosols (e.g., Creamean et al., 2013; Wiacek et al., 2010); it is also the basis of intentional glaciogenic cloud seeding (e.g., Vonnegut, 1947; Mielke et al., 1970; Hobbs and Rangno, 1979).

The 2010 World Meteorological Organization (WMO) report on weather modification states “the glaciogenic seeding of mixed-phase clouds formed by air flowing over mountains offers good prospects for increasing precipitation in an economically-viable manner under suitable conditions” (WMO, 2010). But both actual seeding impact and suitable conditions remain poorly understood (National Research Council, 2003; Garstang et al., 2005). Much research has been conducted into the impact of glaciogenic cloud seeding of cold-season clouds over the mountains in the western United States and elsewhere, mostly using statistical techniques (e.g., Elliott et al., 1978; Mielke et al., 1981; Gabriel, 1995; Manton and Warren, 2011). Several case studies have reported a change in surface precipitation and/or in radar reflectivity following the injection of AgI nuclei (Hobbs et al., 1981; Super and Heimbach, 1988; Super and Boe, 1988; Deshler and Reynolds, 1990; Holroyd et al., 1995; Super, 1999; Huggins, 2007), although attribution is uncertain. Modeling work has shown that natural variability of precipitation can easily overwhelm the seeding effect (Seto et al., 2011; Chu et al., in review). The high variability of precipitation even at the finest spatial and temporal scales remains the biggest challenge in any attempt to observationally isolate a seeding signature (Garstang et al., 2005; Pokharel and Geerts, accepted for publication). The 2010 WMO report states that “if it were possible to predict precisely the precipitation from a cloud system, it would be a simple matter to detect the effect of artificial cloud seeding on that system”.

The most recent research effort to reveal the efficacy of ground-based AgI seeding of orographic clouds is the 2008–2014 Wyoming Weather Modification Pilot Project (WWMPP) (Breed et al., 2014), which focuses on the Sierra Madre and Medicine Bow ranges in southern Wyoming. The 2012–13 AgI Seeding Cloud Impact Investigation (ASCII) project built on the WWMPP, with the specific aim to use new observational tools such as an airborne mm-wavelength radar (Geerts et al., 2013) and Large Eddy Simulations that resolve cloud processes including ice nucleation by AgI nuclei (Xue et al., 2013), to investigate the cloud-microphysical response to glaciogenic seeding.

Commonly used criteria for seeding wintertime orographic clouds with AgI nuclei relate to temperature, presence of supercooled liquid water, and wind direction (Vardiman and Moore, 1978; Breed et al., 2014). The suitable temperature range for AgI seeding in cloud is about  $-8$  to  $-23^{\circ}\text{C}$  (Grant and Elliott, 1974). The lower temperature limit is variable and is dictated by the concentration of natural IN or large aerosol particles in the upstream air. The higher temperature limit

varies somewhat as well, and relates to the temperature dependency of the AgI activation, measured as the number of crystals yielded per gram of AgI. This activation decreases by 2.5 orders of magnitude between  $-10$  and  $-6^{\circ}\text{C}$  (DeMott, 1997). The success of AgI seeding may be affected also by the liquid water content (LWC) and drop size distribution, by the abundance of ice crystals, and by vertical cloud structure. For instance multi-layer clouds with ice crystals falling from aloft onto the shallow orographic cloud may not be suitable.

Natural production of ice crystals from the ground, mixed turbulently within the boundary layer (BL), may also affect the efficacy of ground-based glaciogenic seeding (Rogers and Vali, 1987; Geerts et al., 2011). Depending on the condition of the snow at the surface and in trees, ice crystals may be lofted and mixed into cloud when the wind is strong enough (Kristovich et al., 2012). On the one hand, the depth of the well-mixed BL is important for the mixing of ground-released AgI nuclei into cloud, and this depth is controlled by low-level wind speed and temperature lapse rate. A sufficiently strong cross-barrier wind and large lapse rate are important to avoid blocked flow. On the other hand, natural blowing snow may overwhelm any impact of ground-released AgI nuclei. Thus, relatively weak winds and some low-level potential instability, leading to shallow cumulus clouds, may be optimal, as it avoids blowing snow, ensures low-level flow over (rather than around) the mountain, and allows the mixing of ground-released AgI nuclei into cloud.

The present paper is the second ASCII case study, focusing on shallow orographic convection. The first ASCII case study (Pokharel et al., 2014, hereafter referred to as PGJ14) examines a precipitating stratiform cloud observed under much stronger wind on 21 February 2012 over the Sierra Madre. The cumulative evidence of three complementary radar systems, each with a (quasi-)simultaneous control and target region, indicates a measurable impact of seeding on low-level reflectivity in the PGJ14 case. The most convincing evidence in that case comes from the mapped change in average low-level reflectivity from a Doppler on Wheels (DOW) radar.

Many previous weather modification experiments have deployed one or more radars, as radar reflectivity is a reasonably good measure of precipitation rate. This paper is an observational case study that uses the same radars as the PGJ14 study. The objective of this paper is to detect an impact of ground-based seeding on snow in a shallow winter storm with cumulus convection. The experimental design and instruments are described in Section 2. The storm is described in Section 3. Reflectivity data from the various radars are explored in Section 4. Changes in snow size distribution at the surface and at flight level are described in Section 5. The findings are summarized in Section 6.

## 2. Experimental design and instrumentation

The ASCII-12 project is described in Geerts et al. (2013). The experiment was designed to measure clouds and precipitation initially during natural conditions, and later with three AgI generators in operation. Measurements were collected both upstream and downstream of these generators. The upstream measurements (“control”) are essential in order to monitor the natural variations. The downstream

data (“target”) are examined in the context of the upstream evolution. In some cases near-surface radar data are available over the mountain, to the side of the target area (north and south of the likely tracks of the AgI plumes over the mountain). These data are treated as “lateral control”, with the caveat that the AgI trajectories are not known.

The measurement sites as well as the fixed aircraft flight tracks in ASCII-12 are shown in Fig. 1. The instruments that are used in this case study are described below.

### 2.1. UWKA instrumentation and flight tracks

The University of Wyoming King Air (UWKA) was equipped with the profiling 95-GHz (W-band) Doppler Wyoming Cloud Radar (WCR), the 355 nm Wyoming Cloud Lidar (WCL) and several in situ cloud physics instruments (Wang et al., 2012). The WCR reflectivity profiles are the most useful for this paper's objective, as they depict storm vertical structure from echo top down to ~30 m above ground level (AGL). We also examine data from three in situ particle probes, since flow conditions (convective updrafts and weak winds) support the possibility of AgI nuclei (or nucleated ice crystals) transport up to flight level. The Cloud Droplet Probe (CDP) provides the size distribution of droplets in the 2–50  $\mu\text{m}$  size range. The CDP has a fine spectral resolution and does not suffer from contamination due to ice shattering (Korolev et al., 2013). The two other probes are the Cloud Imaging Probe (CIP) and the 2D-P, both optical array probes, imaging and sizing particles in the 12–2500  $\mu\text{m}$  range and 0.2–20.1 mm ranges respectively.

During the Intensive Observation Period (IOP) of 13 February 2012, the flight level was maintained at 13 kft, i.e., about 930 m above Battle Pass. A series of five geographically fixed aircraft tracks (the “ladder”, Fig. 1) was flown four times. One of these flight tracks (labeled track #1 in Fig. 1)

was upstream of the AgI generators, thus serving as a control measurement. The four flight tracks downstream of the generators (tracks #2–5) are treated as target. Tracks #2 and 3 are located on the upwind side of the mountain, track #4 roughly follows the Sierra Madre crest, and track #5 is in the lee. Two ladders were flown before AgI generator activation at 2015 UTC. This period is referred to as the untreated period, or simply “NOSEED”, for UWKA data (Table 1). By design, a buffer of 38 min was allowed between the AgI generator activation time and the start of the 3rd ladder, to enable the dispersal of the seeding material across the mountain. The winds were weaker on 13 February than in any other ASCII-12 IOP save one, and the soundings' mean wind vector, calculated between the surface and mountain top level, suggests that AgI nuclei could not reach the farthest flight track (track #5) until 55 min after release time. Thus track #5 on ladder #3 is included in the UWKA NOSEED period. The remaining nine tracks in the last two ladders are referred to as SEED (Table 1). All four ladders plus the buffer period (during which time an along-wind leg was flown) were flown in 2.7 h.

### 2.2. Instruments and snow sampling at Battle Pass

Several instruments were operated near Battle Pass, a continental divide pass (elevation 3034 m MSL) located downstream of the three AgI generators (elevation ranging from 2431 to 2551 m). A scanning dual-polarization X-band radar, one of the DOWs for the Center for Severe Weather Research, was located at the pass. The DOW conducted full-volume scans starting at  $-1^\circ$  elevation, and vertical transects along the direction of the low-level wind, cycling every 10 min. A vertically-pointing Ka-band Micro-Rain Radar (MRR) was located about 500 m downwind of Battle Pass at an opening in the forest, named “Battle Town site”

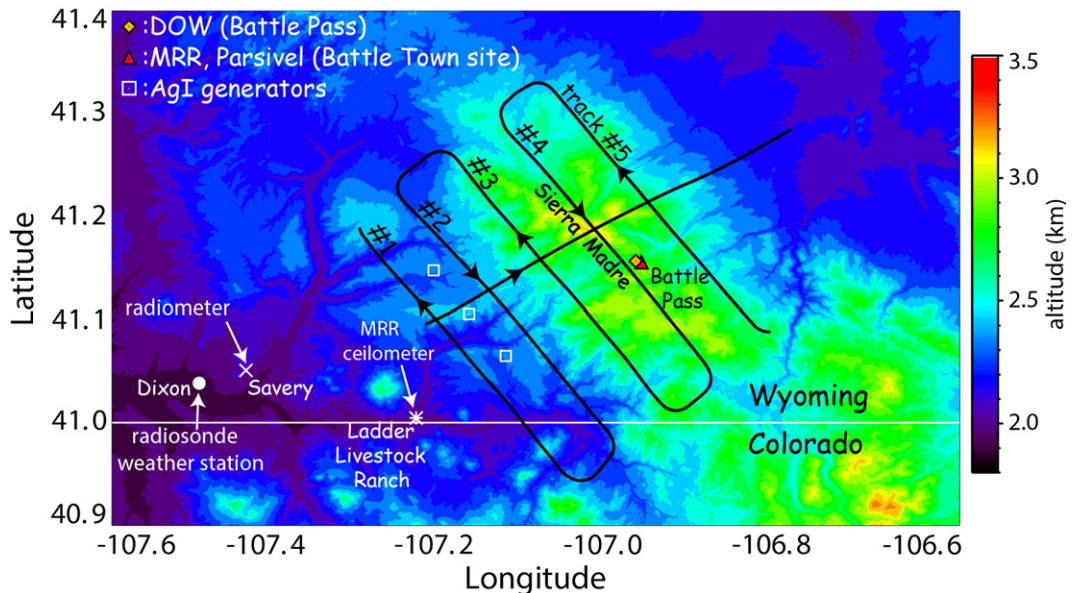


Fig. 1. ASCII-12 experimental design map, showing UWKA flight tracks and ground-based instruments. The terrain elevation is shown in the background. The solid black lines show the UWKA ladder pattern with track labels (#1–5).

**Table 1**

Definition of NOSEED and SEED periods for the 13 February 2012 IOP. Three AgI generators (Fig. 1) were operating from 2015 to 2215 UTC  $\pm$  a few minutes. The times are in UTC (HH:MM:SS). L refers to a ladder pattern, consisting of 5 tracks (T), as shown in Fig. 1. A buffer period between NOSEED and SEED is assumed for the UWKA (2058–2100 UTC) and for the DOW (2058–2100 UTC), but not for the instruments at Battle Town site.

Instrument	NOSEED		SEED	
	Start	Stop	Start	Stop
WCR/UWKA	19:22:30	20:58:07	21:00:33	22:04:03
UWKA cross-wind tracks	L1: T5–T1		L3: T4–T1	
	L2: T5–T1		L4: T5–T1	
	L3: T5			
MRR	19:00:00	21:00:00	21:00:01	23:00:00
Parsivel	19:00:00	21:00:00	21:00:01	23:00:00
DOW	18:53:49	20:58:03	21:00:25	23:09:27

(Fig. 1). A second MRR and a ceilometer were located in a valley about 10 km upstream of AgI generators, at Ladder Livestock Ranch.

Other snow measuring instruments, including a Parsivel disdrometer and several Environmental Technology Inc. (ETI) snow gauges, were operated at or near Battle Town site. A Parsivel disdrometer is an optical sensor with laser diode; it measures snow particle concentration as a function of size and as a function of fall velocity. The instrument measures the maximum diameter of the 1D projection of the particle, which is smaller than or equal to the actual maximum diameter (Yuter et al., 2006). The diameters are binned in 32 bins, ranging from 0.062 mm to 24.5 mm. The lower two size bins are so noisy that only the 30 larger size bins are analyzed.

To verify that snow falling at Battle Town site was impacted by AgI seeding, fresh snow was sampled over four periods during this IOP. The concentrations of Ag and four other trace elements [Rb (Rubidium), Ba (Barium), Sr (Strontium) and Ce (Cerium)] in these snow samples were analyzed at the Desert Research Institute. The concentration of elemental silver in fresh snow varies considerably at synoptic time scales (on the order of days and weeks) depending on atmospheric aerosol loading, aerosol source regions, etc., but it correlates strongly with that of the four other trace elements. Therefore, in an attempt to isolate the presence of artificial Ag in snow, we examine the ratio of the Ag concentration to the concentration of these trace elements. This ratio, termed  $R$ , is defined as:

$$R = \left[ \frac{\text{Ag}}{(\text{Rb}/30)} \times \frac{\text{Ag}}{(\text{Ce}/30)} \times \frac{\text{Ag}}{(\text{Sr}/500)} \times \frac{\text{Ag}}{(\text{Ba}/500)} \right]^{0.25} \quad (1)$$

Each element symbol represents the concentration of that element in ppt units. The scaling is done so that  $R$  becomes approximately equal to one under natural conditions with high aerosol loading. So, when  $R \gg 1$ , it is more likely that silver is being contributed to the snowpack by a non-dust source, such as from AgI nuclei. This criterion has been tested on hundreds of snow samples collected in Wyoming and elsewhere.

### 2.3. Other instruments

Three rawinsondes were released from Dixon, in a valley upwind of the Sierra Madre (Fig. 1), at an  $\sim$ 1-hour interval. The sounding data are used to monitor the vertical structure of the atmosphere, in particular the profiles of humidity, temperature, and wind. An automated weather station provided one minute weather data in Dixon, and a passive microwave radiometer operated in Savery, both west of the Sierra Madre. The radiometer monitored liquid water path (LWP) along a slant path pointed towards the Sierra Madre at elevation angles of 9 and 12°.

## 3. Atmospheric conditions and cloud characteristics

### 3.1. Large-scale conditions and cloud evolution

On 13 February 2012 (IOP #9 in ASCII-12, Geerts et al., 2013), the Sierra Madre was in a polar air mass with low temperatures aloft and a rather low tropopause at  $\sim$ 300 mb. The flow aloft was weak, and the troposphere was rather quiescent, with the nearest upper-level short-wave troughs rather remote, one over California and another over eastern Oklahoma. The middle and upper troposphere were cloud-free. Light wind and high relative humidity were observed at weather stations in the plains around the target area. Shallow clouds and light precipitation occurred over the Sierra Madre, but it remained dry over the surrounding plains.

DOW and WCR data (discussed in Section 4 below) as well as footage from a forward-looking camera aboard the UWKA indicate that shallow convection was present during the 13 February 2012 IOP, especially upwind and over the Sierra Madre. Between 1900 and 2030 UTC this convection was quite weak, and embedded in very light stratiform precipitation. Between 2030 and 2300 UTC it became more intense, slightly deeper, and more isolated. The highest cloud tops were only 4.8 km MSL, yielding a maximum cloud depth of just  $\sim$ 2.4 km, measured from cloud base to WCR echo top. A convective texture became apparent in GOES visible satellite imagery only towards the end of the IOP, when the sun was lower and convective cells became separated by clear sky. This convective texture was not very obvious, and was present only over the mountains. The evolution of this convection coincides with the transition from NOSEED to SEED (Table 1), which complicates the analysis.

### 3.2. Atmospheric profiles upstream of the mountain

The three upwind soundings during the 13 February IOP (Fig. 2) reveal an  $\sim$ 0.5 km deep well-mixed boundary layer, and a nearly moist-neutral layer above that, up to  $\sim$ 580 mb ( $\sim$ 4.5 km MSL). The vertical structure of the troposphere changes little from the first to the third sounding. The low-level wind speed (between the surface to 700 mb) and wind shear are unusually low compared to other ASCII IOPs (Geerts et al., 2013). The low-level wind speed decreases somewhat from  $\sim$ 6 to  $\sim$ 4 m s $^{-1}$  during the IOP. The 660–735 mb layer reaches water saturation in the third sounding (at 2201 UTC), implying that this layer is super-saturated with respect to ice, whereas the two earlier soundings are at

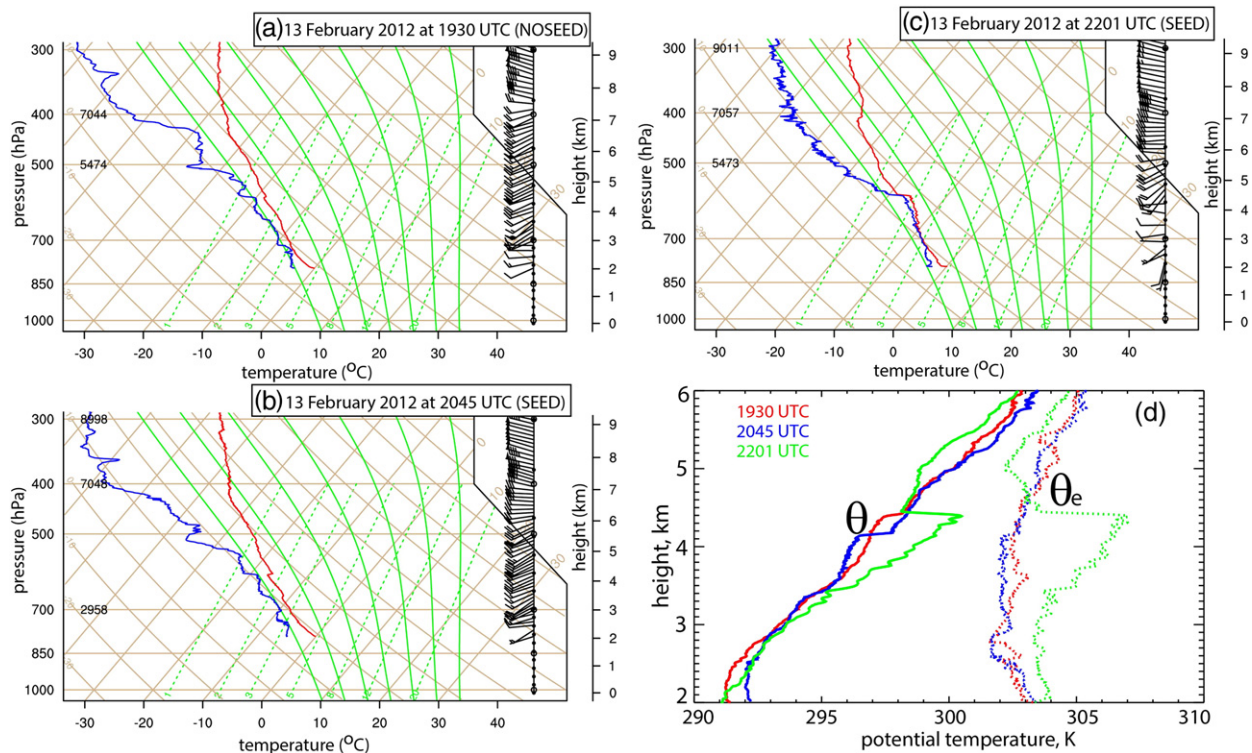


**Fig. 2.** Skew T log p display of rawinsonde data from Dixon (a) during the NOSEED period (1930 UTC), and (b) and (c) during the SEED period (2045 and 2201 UTC, respectively). The red lines show the temperature and the blue lines show the dew point. A full barb equals  $5 \text{ m s}^{-1}$  ( $\sim 10$  kts). (d) Vertical profiles of potential temperature  $\theta$  and equivalent potential temperature  $\theta_e$  for these three soundings.

most saturated with respect to ice, but sub-saturated with respect to water. Another distinct feature from the third sounding is that both temperature and dew point decrease sharply with height at  $\sim 4.5$  km MSL. The anomalous cooling (in excess of the dry adiabatic lapse rate) is due to sublimation of ice as the rawinsonde exits the cloud. The water-saturated layer below cloud top is moist-adiabatic. DOW base reflectivity data suggest that this rawinsonde penetrated a convective cell.

Each of the three upwind soundings reveals potential instability in the lowest 1 km AGL, although equivalent potential temperature  $\theta_e$  decreases by only  $\sim 1$  K with height (Fig. 2d). Here  $\theta_e$  is computed using equation (2.34) in Markowski and Richardson (2010). The middle sounding (at 2045 UTC) is least stable, as the increase in potential temperature  $\theta$  from the surface to 2 km AGL is smallest, and the decrease in  $\theta_e$  over the same depth is largest. Because the third sounding appears to have penetrated a convective cell, potential instability in the environment cannot be evaluated. In other words, convection is most likely around or after 2045 UTC. This convection remains shallow as atmosphere becomes rather stable above 5.0 km AGL.

### 3.3. Storm conditions and evolution during the IOP

We now examine storm evolution in terms of an array of parameters measured at different locations (Fig. 3). The reasons for this analysis are not only to describe storm and

ambient conditions, but also to ascertain that no significant changes occurred during the four-hour IOP in which the seeded period is compared to the untreated period. The NOSEED (SEED) period at Battle Town site is 1900–2100 UTC (2100–2300 UTC) (Table 1). This is based on an estimated advection time from the AgI generators to Battle Town site of 45 min. No buffer period is assumed because the observations are at a single location, unlike the DOW and WCR data.

The surface wind speed at Battle Pass ( $10\text{--}14 \text{ m s}^{-1}$ ) is over twice that in the free atmosphere at the same level (700 mb) just upwind of the Sierra Madre (Fig. 3a). It is stronger also than the surface wind at the reporting AgI generator sites, all of which recorded wind speeds below  $10 \text{ m s}^{-1}$ . DOW radial velocity data (not shown) show that the low-level wind accelerates towards Battle Pass and continues to be strong in the lee. A surface wind speed of  $10 \text{ m s}^{-1}$  is a commonly used threshold for blowing snow (Kristovich et al., 2012). This, plus the absence of significant blowing snow (visual observations around Battle Pass) implies that competition with wind-driven natural ice initiation arising from the ground is unlikely during this IOP. This is an important factor in the choice of this case study.

The temporal changes of wind and temperature during the IOP are very small (Fig. 3a and b), confirming the absence of any frontal passage. The slight surface cooling at Battle Pass may simply be diurnal. The bulk Brunt–Vaisala frequency  $N$  shown in Fig. 3d applies to a parcel ascending from the

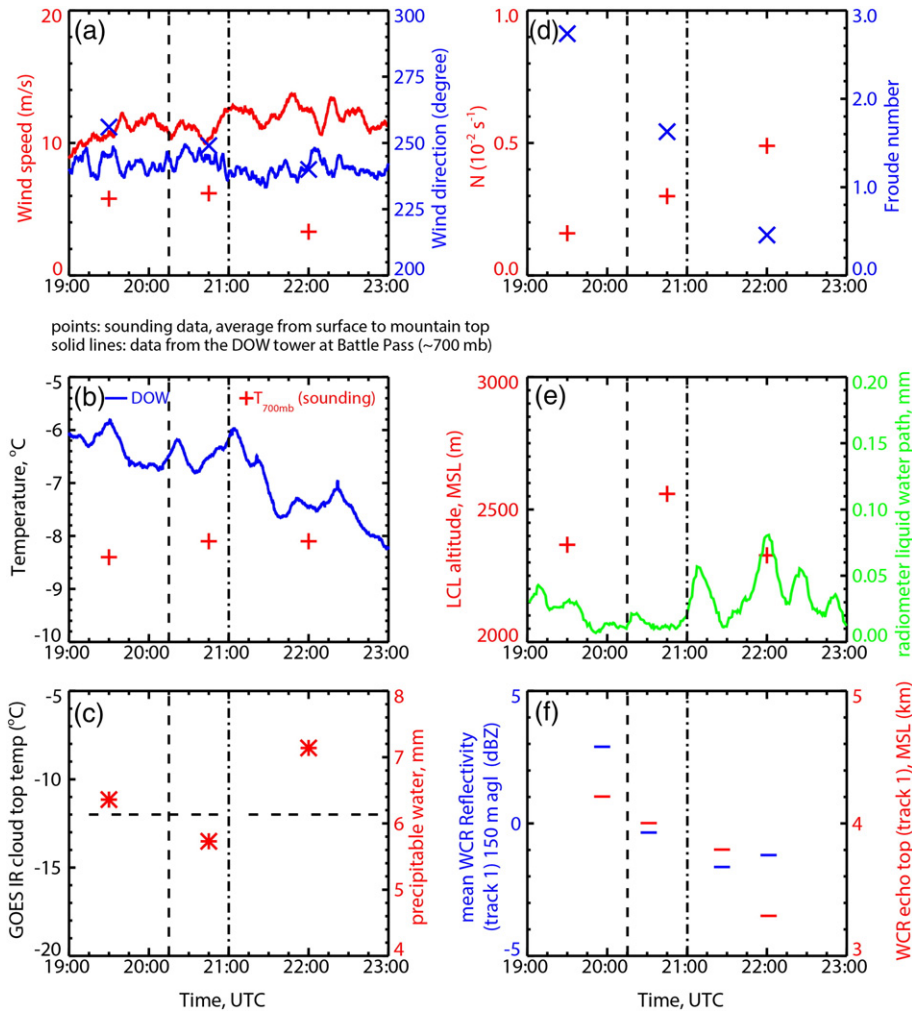


**Fig. 3.** Evolution of several atmospheric parameters during the course of the IOP on 13 February 2012, as measured by rawinsondes, weather stations in the upwind valley and on the mountain, WCR, and satellite. The vertical dashed line and vertical dashed-dotted line in all panels show the AgI generators start time and the estimated arrival time of the AgI plume at Battle Pass, respectively.

surface to mountain top level. It is the dry value below the lifting condensation level (LCL) and the moist value above. The moist Brunt–Vaisala frequency is computed following Kirschbaum and Durran (2004). This  $N$  and the surface-to-mountaintop mean wind speed  $U$  are used to compute the bulk Froude number  $Fr$  [ $Fr = U/(NH)$ , where  $H$  is the height of the mountain above the upwind plains]. The stability  $N$  is rather low (Fig. 2), yet  $Fr$  is not very large, on account of the weak wind. Still,  $Fr$  is larger than unity for the first and second soundings and the surface wind directions at Dixon, at the AgI generators, and at Battle Pass all remain between 230 and 260°, suggesting that the air within the upwind boundary layer is advected over the mountain during the IOP, rather than blocked.

Precipitable water (calculated from soundings) also remains rather steady during the IOP, showing first a decrease and then an increase, from ~6 to ~7 mm (Fig. 3c). This change in precipitable water is consistent with the change in LCL (Fig. 3e), and with the increase in radiometer LWP around the time of the 3rd sounding (Fig. 3e). The

average LCL is about 2430 m MSL, which is close to the mean ceilometer cloud base height (2510 m MSL) measured at Ladder Livestock ranch (Fig. 1), and close to the average terrain height at the AgI generator sites (2480 m MSL). This implies that AgI nuclei released from the generators quickly find themselves in cloud. The temperature near the generators is rather warm for AgI activation, but the temperature is at or below  $-8$  °C deeper in the boundary layer and over higher terrain (Fig. 3b). This is a better temperature range for AgI-induced ice nucleation (DeMott, 1997). The radiometer LWP values (0.03 mm on average, Fig. 3e) are rather low compared to the average value of 0.12 mm for all ASCII-12 IOPs (Geerts et al., 2013). The spikes in LWP during SEED are due to shallow convection passing through.

We also examine WCR echo top and mean low-level reflectivity along track #1 (Fig. 3f). The purpose is to examine typical cloud depth and snowfall rate, and any changes during the IOP, in an area unaffected by seeding, just upwind of the AgI generators. The caveat of this analysis is that the sample size is small (only four passes), and WCR profile

measurements along each pass may not be fully representative, especially if precipitation is spatially non-uniform (showery). In any event, the WCR echo top is about 4.2 km along track #1, implying a mean cloud depth (LCL to top) of 1.7 km. The WCR mean echo top and the snowfall rate in the control region decreased slightly during the IOP (Fig. 3f). The echo top topography along other tracks also becomes more uneven, as will be shown later.

In short, the environment and storm on 13 February 2012 were relatively steady during the IOP, and supercooled cloud droplets were present between the generators and the downwind Sierra Madre crest. These observations bode well for the detectability of a seeding signature. Only subtle, small environmental changes during this IOP explain the transition to shallow convection, which will be documented in Section 4.

#### 3.4. Orographic cloud and precipitation structure on a flight transect across the mountain

Measurements from different airborne instruments for a flight leg oriented along the mean low-level flow, across the mountain, are shown in Fig. 4. This along-wind leg was flown during the buffer period following the completion of two ladder patterns (Fig. 1), about the time of the 2nd sounding, which was least stable (Fig. 2). Ascent is evident upwind of the mountain, and subsidence dominates in the lee (Fig. 4b). Shallow terrain-driven eddies can be seen around smaller ridges. Spectral analysis of the WCR vertical velocity near the ground (not shown) suggests little turbulent kinetic energy in the boundary layer, compared to measurements from other ASCII storms in this area (Geerts et al., 2011), consistent with the weak winds on this day. Thus boundary layer mixing was rather slow, and confined to a shallow depth, ~500 m.

Shallow convective towers with strong upper-level updrafts are evident in this transect, mainly in the lee (e.g., at 2046–2047 UTC in Fig. 4b). They are important because it enables vertical transport of air (including AgI nuclei) that would otherwise remain contained in the shallow boundary layer.

We are focusing for a moment on the main convective tower observed in the lee, at 2046–2047 UTC. It contains relatively copious liquid water (Fig. 4e) and numerous ice crystals (Fig. 4f), suggesting significant snow growth. The tower contains small updraft regions near cloud top, surrounded by downdrafts. Interestingly, these updrafts correspond with pockets of high reflectivity surrounded by much lower values (Fig. 4a). These are similar to “generating cells” observed near the cloud top of frontal systems (Rosenow et al., 2014; Plummer et al., in review). These generating cells also appear to be due to the release of potential instability. The upshear western side of these small cells in our transect has stronger updraft cores (Fig. 4b), with large values of LWC, up to  $0.6 \text{ g kg}^{-1}$  and  $160 \text{ droplets cm}^{-3}$  at flight level (Fig. 4e), while the older eastern side has higher reflectivity and thus larger crystals (Fig. 4a).

Another shower with convective updrafts, turbulence and high LWC is evident further upstream, at flight time ~2041 UTC. While there is broad ascent across the upwind side of the mountain, convective motions clearly are also present

there. In general, convection is important in the distribution of liquid water, snow, and thus precipitation.

On the upwind side of the mountain, mainly between 2042 and 2043 UTC, narrow sections of high nadir lidar backscatter power and rapid, near complete attenuation of the lidar signal beyond can be seen in Fig. 4c. This indicates the tops of shallow liquid clouds below flight level. These clouds deepen towards the mountain crest. The LWC is high ( $\sim 0.5 \text{ g kg}^{-1}$ ) in the cloud that reaches flight level near 2043:15 UTC (Fig. 4e). Its concentration of small ice crystals is high as well,  $\sim 300 \text{ L}^{-1}$  (Fig. 4f), but the cloud lacks snowflakes larger than 1 mm (Fig. 4g), hence the reflectivity is low (Fig. 3a). Generally droplets are small in this cloud and elsewhere, almost all with a diameter below  $30 \mu\text{m}$ , according to CDP measurements (Fig. 4e).

In order to further examine the depth of the orographic liquid water cloud below flight level on the upwind side, the WCL and in situ LWC data along the three upwind tracks (#1, 2, and 3, see Fig. 1) were analyzed. The lidar data generally indicate an increase in cloud top height below flight level from track #1 to track #3, although mixed-phase clouds were encountered at flight level along all tracks (mainly during SEED) with  $0.05\text{--}0.5 \text{ g m}^{-3}$  of liquid water, with the lower values prevailing during NOSEED. This indicates that cloud liquid water was present in the region where the ground-based AgI generators operated.

#### 4. Seeding impact detection: radar reflectivity

Both radars and in situ instruments on the ground and aboard the UWKA are used to characterize cloud and precipitation and to detect any seeding signature. Three radar systems are used, complementary in their viewing perspective and spatial coverage. For all three systems, SEED vs. NOSEED conditions are compared, not only in the target region, but also in control regions, to account for natural storm trends.

##### 4.1. Was the Battle Pass target area impacted by AgI seeding?

The surface wind directions observed at various locations and the DOW low-level radial velocity data suggest that southwesterly flow arising from near the AgI generators was channeled into Battle Pass. Fresh-snow samples collected roughly hourly at Battle Town site during the IOP indicate that snow falling there contains Ag from the AgI generators (Fig. 5). The mean low-level WCR reflectivity (Fig. 3f) and the Battle Town site ETI gauge (Fig. 5a) suggest a very light snowfall rate,  $< 1 \text{ mm h}^{-1}$ , water equivalent. Therefore more frequent sampling was not possible.

The Ag concentration and the factor  $R$  (Eq. (1)) in these samples are shown in Fig. 5b. The first two snow samples were collected during NOSEED, the last two during SEED (Table 1). The 2nd sample (NOSEED) has near-zero Ag and  $R$  values, implying that this snow was not impacted by AgI seeding. The third sample, collected during the early SEED period, is similar to the first one; both are well within the range of natural conditions. The elevated  $R$  value and Ag concentration in the last sample are strong evidence for glaciogenic seeding impact at Battle Town site, since the median Ag concentration for all 2012 samples was approximately 1 ppt.

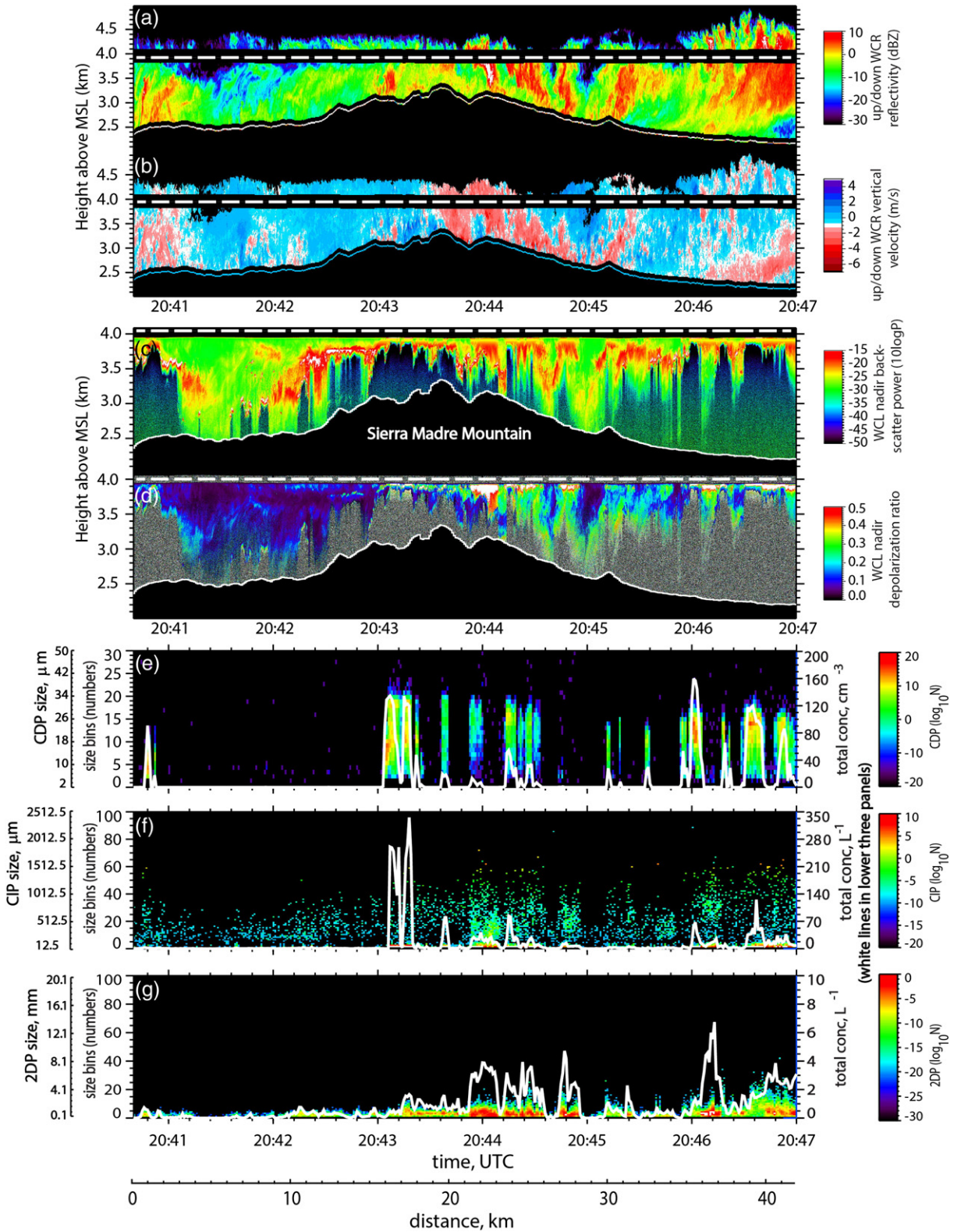


**Fig. 4.** WCR, WCL and in situ probes transect for the along-wind flight leg over the Sierra Madre shown in Fig. 1. The wind direction is from left (260°, west) to right (80°, east). (a) WCR reflectivity and (b) WCR hydrometeor vertical velocity (both above and below the aircraft); (c) WCL backscatter power, (d) WCL depolarization ratio (both below the aircraft only). The dashed white line in panels a–d is the UWKA flight level, and the jagged line below is the terrain profile. The black belt around the dashed white line in panels a–b is the radar blind zone for the zenith and nadir WCR antennas. Corresponding flight-level measurements are shown in panels e–g. (e) Drop size distribution with droplet concentration (solid white line) measured by the CDP; and (f) & (g) ice size distribution with total ice concentration (solid white lines) measured by the CIP and 2DP, respectively.

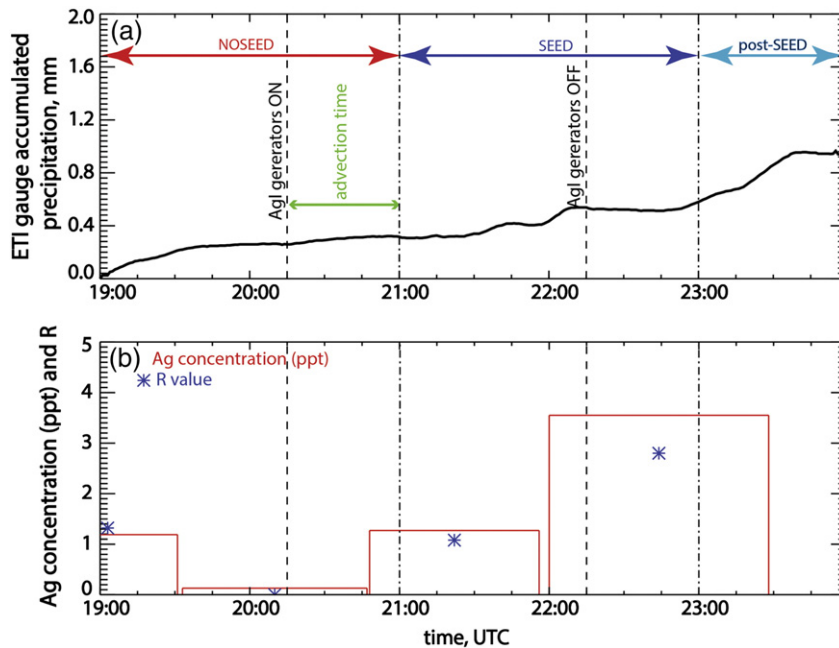


**Fig. 5.** Time series of (a) accumulated precipitation measured by a ETI snow gauge, and (b) silver concentration, Ag, in parts per trillion (ppt) and the factor R from four snow samples collected during the IOP. The width of the histogram shows the duration of snow sample collected. The first snow sample collection started at 18:35 UTC. The measurements are from Battle Town site.

This sample includes snow that fell in the early “post-SEED” period. It is possible that typical advection time between the AgI generators and the pass is longer than that inferred from the surface-to-mountain top mean wind, as was the case for the PGJ14 case study.

In short, there is strong evidence that the snow falling in the Battle Pass target area was impacted by AgI seeding.

#### 4.2. Wyoming Cloud Radar

Four WCR reflectivity transects are shown in Fig. 6, each one along track #4. This track was flown along the crest of the Sierra Madre and is about 15 km downstream of the AgI generators, corresponding to ~40 min of advection time on this day. The upper (lower) two panels in Fig. 6 are during the NOSEED (SEED) period. The asterisk symbols below the terrain show the projected locations of the AgI generators, assuming the direction of the mean wind at low levels. The overall precipitation structure indicates that the storm becomes shallower during the SEED period, but convection becomes dominant. The same transition from mostly stratiform to mostly convective precipitation can be seen along the four other tracks (not shown). The convective cells have updrafts up to  $4 \text{ m s}^{-1}$ , LWC up to  $0.5 \text{ g m}^{-3}$ , and echo tops up to 5.0 km MSL. One could hypothesize that the transition from mostly stratiform precipitation to mostly convective precipitation is a dynamic seeding impact in a marginally unstable environment (Bruintjes, 1999). This hypothesis is likely false, because convective activity is seen along the control track (#1) and across the domain scanned by the DOW (Section 4.4), and the convective cells are not located downwind of the AgI generators in the WCR transects (Fig. 6c and d).

In order to contrast NOSEED and SEED periods, WCR reflectivity from all target tracks (tracks 2–5) is composited into frequency-by-altitude diagrams (FADs) (Yuter and Houze, 1995) for the two periods (Fig. 7). These diagrams show the normalized frequency of reflectivity values by height AGL. Since AgI seeding is ground-based and to a first order low-level flow advected over a mountain follows the terrain, the height is shown AGL. The cloud is clearly deeper during NOSEED (Fig. 7a) than during SEED (Fig. 7b) on average. The convective cells observed during SEED result in a bimodal distribution of reflectivity above 0.7 km AGL. Thus the probability of reflectivity  $\geq 10 \text{ dBZ}$  is greater during SEED at all levels (Fig. 7c). The broader spread of low-level reflectivity values during SEED results in two maxima in the reflectivity difference FAD, at low and at high reflectivity. The average reflectivity change (solid vs. dotted line in Fig. 7c) is very small, too small to draw any conclusions, since small displacements of convective cells during SEED relative to the tracks can significantly impact the mean.

Matching WCR FADs for the upstream control track (#1) are shown in Fig. 7d–f. These FADs are based on a smaller sample size and thus are less significant than those for the target region (one vs. four tracks), but a thinning and weakening of the background echo and the development of a bimodal (i.e. convective) reflectivity distribution during SEED is apparent in the control region as well, although the convection is not nearly as strong: the mean low-level reflectivity increases by ~4 dBZ from Fig. 7e to b, which may simply be an orographic effect. But the increase in mean reflectivity from track #1 to the tracks closer to the mountain crest is not as large earlier, during NOSEED. In effect, the storm is thinning and weakening at all levels in the control region, and the convection during SEED is so weak that the

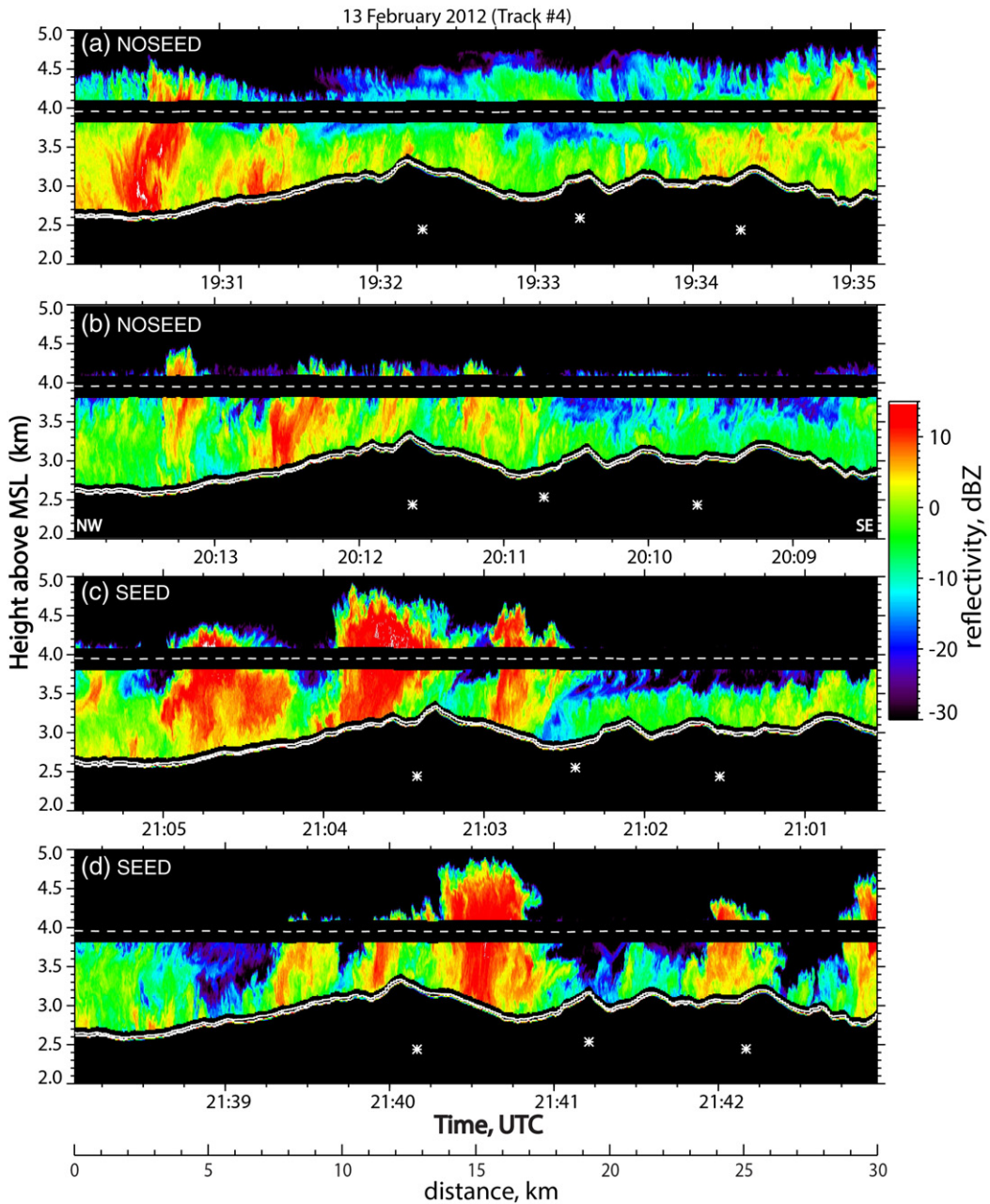


**Fig. 6.** Example UWKA radar reflectivity transects, collected along flight track #4 (Fig. 1) on 13 February 2012. All transects are from NW (left) to SE (right). The upper two transects were flown during the NOSEED period, and the lower two transects during the SEED period. The asterisks in all panels show the location and actual elevation of the three AgI generators (21 km into the page) projected onto this transect.

reflectivity difference FAD (Fig. 7f) does not show the low-level tripole that is seen in target region (Fig. 7c).

Evidence from the WCR data analyzed so far fails to reveal a clear seeding signature. Therefore we further explore the WCR reflectivity profiles. One issue regards fetch, or growth time. Super and Heimbach (1988) observed more snowfall enhancement within 4 km downwind of ground based generators. But Holroyd et al. (1995) observed that snowfall increases mostly farther downwind of AgI generators on the ground. These contradictory results may be due to the

different atmospheric conditions during these experiments. In our case, since it takes time for ground-released AgI nuclei to be advected into convective clouds, and time for the resulting snow to fall to the ground, we hypothesize that at close range (tracks #2 and #3, corresponding to 10–25 min from release time) seeding increases the reflectivity aloft, into the convective towers, and at greater range (tracks #4 and #5, or 40–50 min) the increase is concentrated near the surface. This is exactly what is observed (Fig. 8a and b). But this SEED–NOSEED reflectivity pattern change can be a

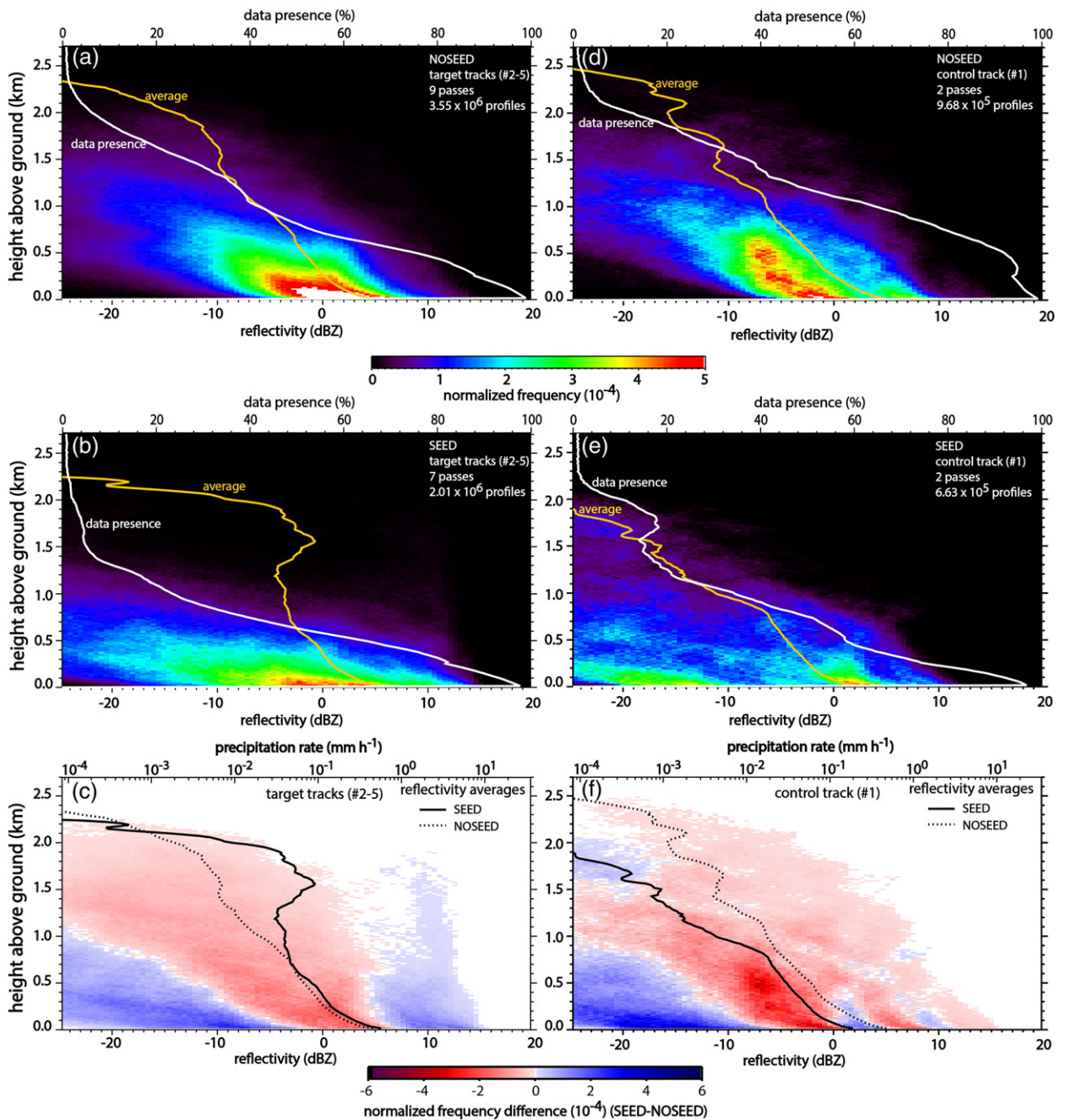


**Fig. 7.** Normalized frequency by altitude diagrams of WCR reflectivity for the flight on 2012/02/13. The left panels apply to the four tracks downwind of the AgI generators (target), and the right panel to track #1 (control). The top panels apply to the NOSEED period, the middle panels to the SEED period, and the bottom panels show the difference (SEED–NOSEED). Also shown are the mean reflectivity profiles (orange lines in the upper four panels, and black lines in the bottom panels) and the “data presence”, i.e. the percentage of WCR range gates with radar echo as a function of height (white line in the upper four panels). The precipitation rate ( $R$ ) shown in the upper abscissa of the bottom panels is inferred from  $R = 0.11 Z^{1.25}$  (Matrosov, 2007).

natural temporal change due to the onset of orographic convection, which tends to grow upwind of the crest (tracks #2 and 3) and discharge its precipitation near or downwind of the crest (tracks #4 and 5).

The possibility remains that convective precipitation, even if its onset was natural, was more intense due to the

incorporation of AgI nuclei into convective updrafts. The curvy bounded weak-echo region below flight level at 2140:40 UTC in Fig. 6d, for instance, corresponds to a 2–3 m s<sup>-1</sup> updraft (WCR Doppler velocity data). This updraft reaches flight level, where some 600 ice crystals per liter were recorded by the CIP. To assess this possibility, we look

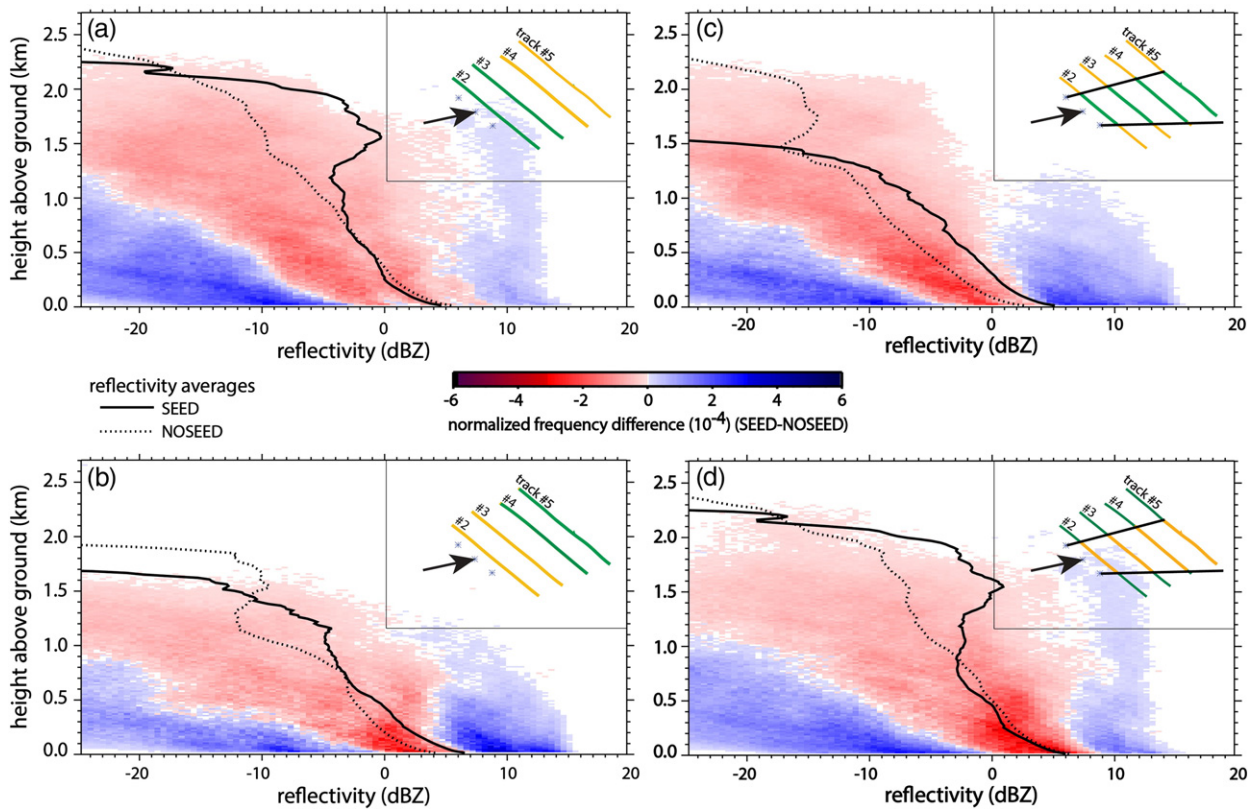


**Fig. 8.** Difference in normalized FAD (SEED–NOSEED) of WCR reflectivity for (a) the two target tracks nearest the generators (tracks #2 and #3), (b) the two more distant flight tracks (#4 and #5), (c) within a cone encompassing the three generators, and (d) outside this cone. In each panel an inset schematic map is shown, with the three AgI generators, the wind direction, and the four target tracks (simplified from Fig. 1). Tracks or track sections that are used in the FAD are colored green.

for a lateral “control” region, since there is some evidence that AgI seeding plumes tend to be rather narrow, both from observations (Holroyd et al., 1988; Huggins, 2007) and from modeling work (Chu et al., in review). We define the lateral control region as that outside a  $20^\circ$  cone region encompassing the three generators (Fig. 8d). The cone orientation is given by the direction of the average low-level wind. For this analysis the sample size in the control region (outside the cone, 47% of the four tracks) is more balanced with that in the target region (within the cone, 53%) than for the upstream control comparison (Fig. 7). The WCR reflectivity difference FAD within the cone reveals a positive low-level dipole (higher probability of high reflectivity at low levels, at the expense of a relatively lower probability of somewhat lower values during SEED), and an  $\sim 3$  dB increase in mean reflectivity in the lowest 1 km (Fig. 8c). Yet no low-level reflectivity increase is observed in the lateral control region between SEED and NOSEED (Fig. 8d). It becomes more difficult to argue that this lateral (along-crest) difference in temporal change is natural as well.

#### 4.3. Micro-Rain Radars

Two MRRs operated during this IOP, one downstream (target) and one upstream (control) of the AgI generators (Fig. 1). The MRR data were reprocessed to remove the noise

following Maahn and Kollias (2012); this usually resulted in the exclusion of the first two range gates. Target and control MRR reflectivity profiles are shown in Fig. 9. Snowfall is more persistent and more intense at the target site at Battle Pass, than at the control site in a valley; in fact there are no measurable echoes above the control site during most of the 4-hour period. It remains dry at the control site during NOSEED and some precipitation develops during SEED. This disagrees with the trend in the WCR control region, i.e. weakening reflectivity from NOSEED to SEED (Fig. 7f). This is not surprising, since snowfall fell in showers, mainly during SEED. Neither track #1 WCR data nor upstream MRR data represent the broader upstream control region (Fig. 1). No snowfall was reported during the IOP further upwind of the Sierra Madre, at the weather station in Dixon (Fig. 1), confirming that this event is purely orographic, and showing the limitations of the upstream control measurements to determine natural trends in precipitation. Both MRRs confirm the development of convective showers during SEED, consistent with the more detailed WCR transects.

The MRR profiles at Battle Pass are synthesized in reflectivity difference FADs in Fig. 9c. This shows that reflectivity is highest near the ground, confirming shallow orographic growth and that the storm is quite shallow. It also reveals an  $\sim 10$  dBZ reflectivity increase from NOSEED to SEED. This increase is much larger than that seen by the WCR

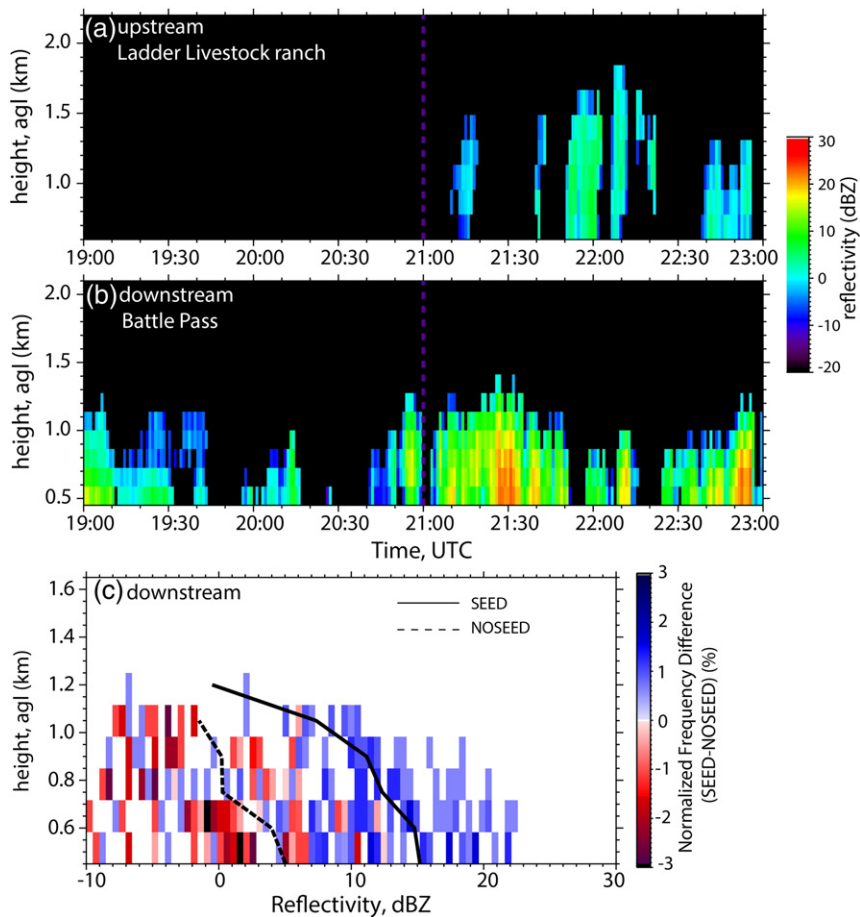


**Fig. 9.** MRR measured reflectivity data from (a) the control site (Ladder Livestock ranch) and (b) the target site (Battle Pass) during the experiment period. The vertical line in both panels shows the start of the SEED period at Battle Pass (Table 1). (c) Difference in normalized reflectivity FAD (SEED–NOSEED) for the target MRR, plus the mean reflectivity profiles for the two periods.

in its target region. It is mainly due to the passage of two convective cells overhead during SEED (Fig. 9b).

#### 4.4. DOW radar

The main strength of the DOW radar data is that they are 3D (volume-scanning), the main limitation is the lack of quality data near the ground in complex terrain. The return power at many radar gates in low-elevation scans is suspect because of ground clutter, specifically, because of side lobes, anomalous propagation, or other interferences with the terrain. Ground clutter is evident in reflectivity or radial velocity animations, even at large range in this case. We remove ground clutter using a fuzzy logic algorithm based on the density function for snow and for ground clutter, following Gourley et al. (2007). Next, the polar coordinate data are interpolated to a Cartesian grid, using Reorder (Oye et al., 1995). Next FADs were constructed. Consistent with the WCR and MRR analysis, the altitude in the FADs is expressed AGL, thus the height of a Cartesian gridpoint is converted first to height above the local terrain. In addition to a dense volume coverage pattern (duration: 8.5 min), the DOW completed some RHI (Range Height Indicator) scans

parallel to the mean low level wind (1.5 min) in most cycles. For the RHIs, the FADs are based on data in their native spherical coordinate system.

Four regions of DOW volume data are defined (Fig. 10). The *upwind control area* is defined as a region upstream of the three Agl generators where lowest unblocked DOW beam is not higher than 1.0 km above the terrain. The *upwind target area* is downstream of the three Agl generators, but upstream from the mountain crest. The *lee target area* is located downstream of the three Agl generators and in the lee of the mountain crest. These two target regions are separated to examine the seeding impact on opposite sides of the mountain, as it allows an assessment of fetch (similar to the WCR comparison of near vs. distant tracks, Fig. 8), and because the two sides are in different river basins. Finally, the *lateral control area* is the area on the side of the upwind target area, similar to the region outside the cone box in Fig. 8d. As for the WCR cone box, the lateral boundaries of the target areas are defined by the mean wind direction plus a dispersion angle ( $\pm 10^\circ$ ) as shown by the bold black lines in Fig. 10. Unfortunately the DOW *lateral control area* is rather small because of beam blockage by higher terrain to the S and NW.

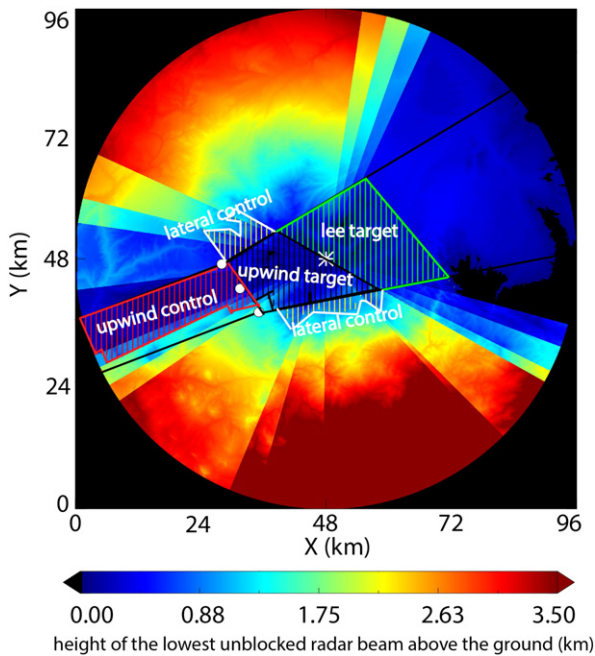


**Fig. 10.** Height (km AGL) of the lowest unblocked beam from the DOW radar, located at Battle Pass (Fig. 1). Also shown are four vertically hatched regions used in the analysis of the seeding impact: the upstream control region (red), the lateral control regions (white), the “close target” region (black) upwind of the mountain crest, and the “lee target” region (light green) in the lee. The control area is defined as a region mostly upstream of the AgI generators where the lowest unblocked DOW beam is no more than 1 km above the terrain.

The resulting DOW reflectivity difference FADs (SEED–NOSEED) are shown in Fig. 11. After ground clutter removal, few data remain below ~500 m, and only in the two target regions, in close proximity to the DOW. The reflectivity increases during the SEED period in all four regions, at all levels (except at upper levels in the *lee target* region). This change is in agreement with the MRR profiles (Fig. 9a), and is consistent with the appearance of convective towers. Because of the DOW’s limited sensitivity (compared to the WCR), no tripole structure appears at upper levels in the FAD, unlike in the WCR data (Fig. 7c). The convection appears to be orographically-driven: reflectivity increases mostly aloft upwind of the mountain where the showers grow (in the *upwind control* and *upwind target* areas). Yet reflectivity increases mostly at low levels in the lee between NOSEED and SEED: the maturing convective towers discharge their snow towards the ground in the *lee target* area, consistent with WCR data along track #5 (Fig. 8b). The high reflectivity values during SEED in the upwind control region are mostly due to a single convective cell moving across the region in the last four DOW volumes of the SEED period. Thus the large SEED–NOSEED difference in Fig. 11c is somewhat by chance.

The same orographic “forcing” should apply to the *lateral control* area, whose average terrain height is about the same as in the upwind target area (Fig. 1). The average reflectivity enhancement is almost the same in this area (Fig. 11d) as in the upwind target area, suggesting that convection emerged there as well. In fact the average reflectivity profiles in the

*upwind target* and the *lateral control* regions during SEED (solid lines in Fig. 11a, d) are about the same. Thus orography is the main driver for convective growth, at a time which happened to roughly coincide with the start of the SEED period.

The total sample size for the RHI-based FADs (Fig. 12) is much smaller than for the volume scans (Fig. 11), because only two RHIs were available to the west, and three to the east (Fig. 13f). The sample size is especially small for the upwind control area because it was intersected by one RHI scan only, and because of the large range, which implies that just a few low elevation angles intersect precipitation. Nevertheless, the RHI-based FADs confirm that low-level reflectivity increased in the target regions, mainly in the lee, consistent with the intensification of shallow orographic convection.

The average low-level reflectivity is mapped in Fig. 13 for the two periods. The alignment and regular spacing of some maxima, esp. during SEED, is due to the movement of convective cells, sampled at 10 minute intervals. (The spacing between the maxima along these lines corresponds with the mean wind speed times the DOW sampling interval.) These estimates are most robust in the target regions close to the radar, and less certain at greater range (Fig. 13c and d). The paucity of data to the north and south is simply due to beam blockage by the higher terrain nearby Battle Pass (Figs. 13f, 10).

The SEED–NOSEED reflectivity difference is mapped out in Fig. 13e. An increase in reflectivity is observed everywhere, except between the convective cells, mainly in the lee. The linear appearance of positive and negative anomalies in this map again is an indication of convective cells drifting with the wind. Fig. 13e suggests that the development of convection during SEED increased low-level reflectivity everywhere. There is no indication of enhanced intensification starting downwind of the three AgI generators, nor is the intensification confined to the nominal width of the AgI plume (i.e., the black lines in Fig. 13e).

#### 4.5. Profiles of radar reflectivity change

Natural variation is the major challenge in discerning a seeding signature; in this case shallow convection emerged or intensified about the time seeding started over the target mountain as the AgI nuclei. PGJ14 devise an expression of reflectivity change in the target area, relative to that in a control area. They define the radar reflectivity impact parameter (ZIP) as the difference between the downstream (target) average reflectivity change (SEED–NOSEED) and that upwind of the AgI generators (control), i.e.

$$\text{ZIP} = \Delta \text{dBZ}_T - \Delta \text{dBZ}_U \quad (2)$$

where  $\Delta \text{dBZ} = \text{dBZ}_S - \text{dBZ}_N$ , and subscript S (N) refers to SEED (NOSEED), while subscript T (U) refers to treated or target (untreated or control).

Given that reflectivity  $Z$  ( $\text{mm}^6 \text{m}^{-3}$ ) correlates rather well with precipitation rate ( $R$ ,  $\text{mm h}^{-1}$ ) at all three radar frequencies, and given our interest in the impact of glaciogenic seeding on  $R$ , we derive another parameter, the precipitation impact factor (PIF), which is defined as a relative change in  $R$  (SEED compared to NOSEED) in the

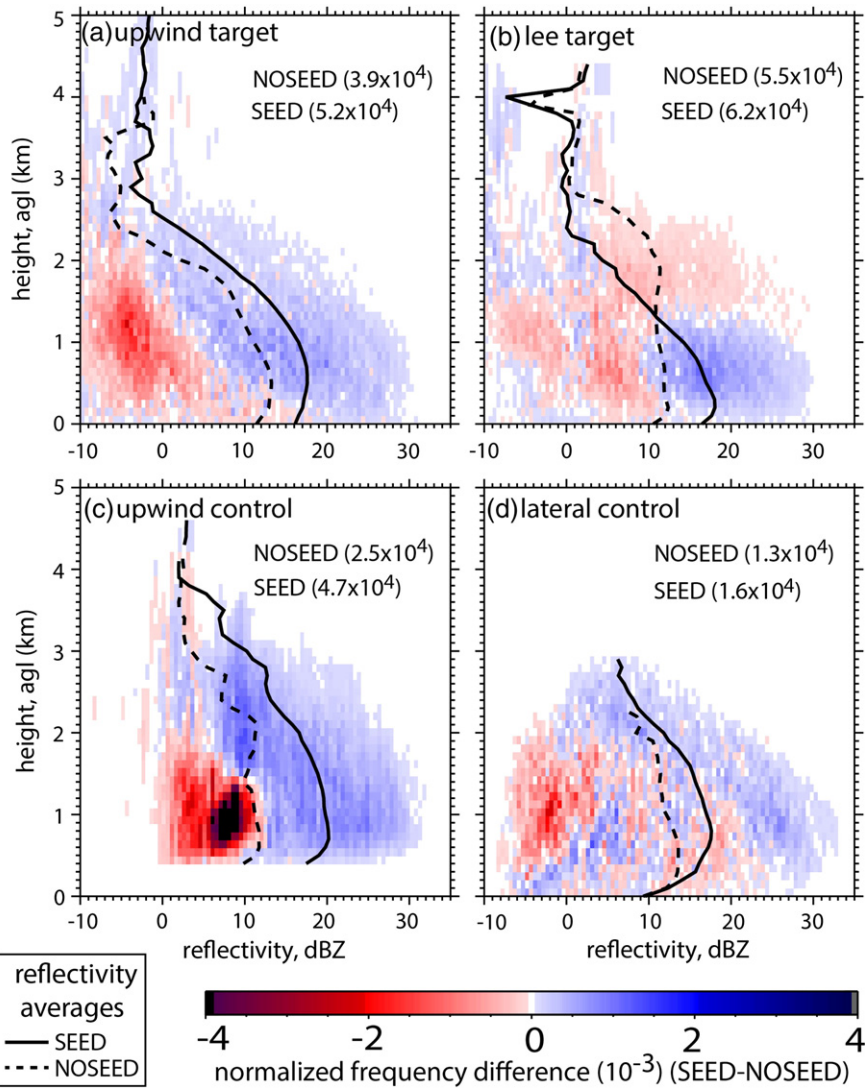


Fig. 11. DOW radar reflectivity difference FADs (SEED-NOSEED) measured in the two control and the two target regions shown in Fig. 10. Solid and dashed black lines in all panels show the average values during SEED and NOSEED, respectively. The total sample size is shown between brackets in each panel, for each of the two periods.

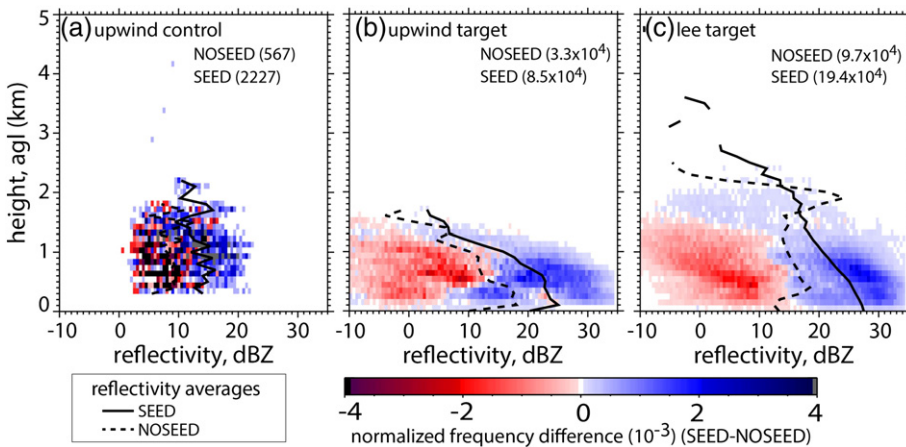
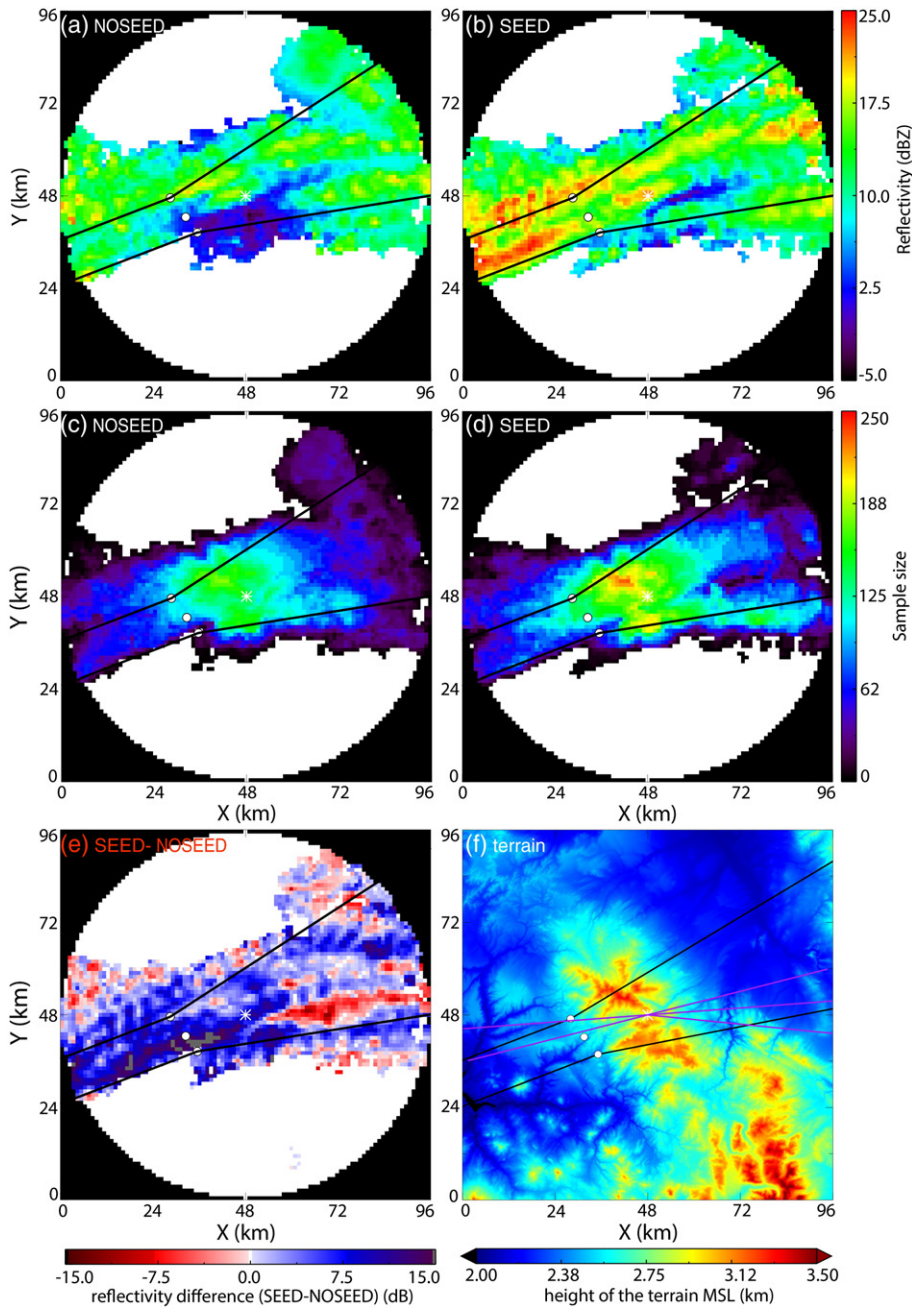


Fig. 12. As shown in Fig. 11, but for the available DOW RHI scans during SEED and NOSEED. The direction of the RHI scans is shown in Fig. 13f (purple lines). No RHI scans transected the lateral control region.



**Fig. 13.** The two upper panels show the average DOW reflectivity below 1.5 km AGL during (a) NOSEED (10 volumes averaged) and (b) SEED (13 volumes averaged). The middle panels show data density, specifically, the number of values contributing to each pixel's average during (c) NOSEED and (d) SEED. (e) Mean reflectivity difference SEED–NOSEED, i.e. (b)–(a). (f) Corresponding terrain map, with the direction of the RHI scans (purple lines). In all these maps, the white circles are the Agl generators, and the black lines indicate the low-level wind direction and, starting at the generators, they outline a dispersion cone  $\pm 10^\circ$  from this direction.

target area compared to the same relative change in the untreated area. PIF is calculated as:

$$PIF = \frac{\frac{R_{S,T}}{R_{N,T}}}{\frac{R_{S,U}}{R_{N,U}}} \quad (3)$$

Assuming the standard Z–R relationship of the form  $R = aZ^b$ , where  $a$  and  $b$  are constants, PIF is related to ZIP, as shown in PGJ14:

$$PIF = 10^{\left(\frac{b \cdot \Delta Z}{10}\right)}. \quad (4)$$

A range of values of  $b$  have been found observationally for cm-wave radars (e.g., Austin, 1987). Table 1 in Rasmussen et

al. (2003) summarizes  $Z$ - $R$  relationships for snowfall from the literature, with values of  $b$  ranging from 0.45 to 0.67. For mm-wave radars including the MRR, theoretical (Matrosov, 2007) and observational (Geerts et al., 2010; Pokharel and Vali, 2011) studies suggest a value  $b = 0.7$ . We use a single value ( $b = 0.7$ ) in Fig. 14, for the simple reason that the emphasis is not on the magnitude of the precipitation change, but rather on its sign. Given Eq. (4) and a single value of  $b$ , the abscissa in Fig. 14a can be expressed in terms of ZIP or PIF. Values of ZIP  $> 0$  (and thus PIF  $> 1$ ) imply a positive reflectivity (snowfall) trend in the target region, relative to the control region, from NOSEED to SEED. While PGJ14 considered ZIP and PIF near the ground only, to quantify the possible impact of glaciogenic seeding on near-surface precipitation rate, these variables can be evaluated at any height (Fig. 14).

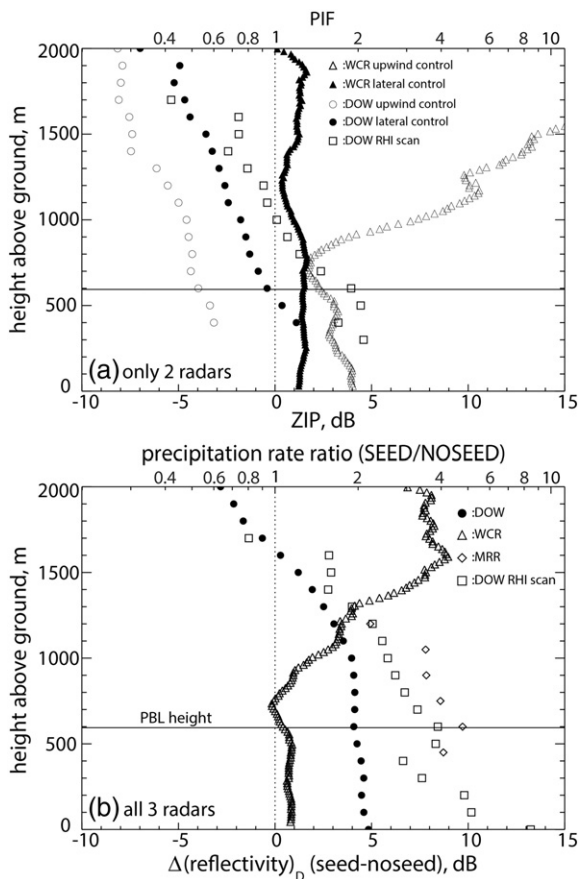


**Fig. 14.** Vertical profile of reflectivity change, according to three radar systems. (a) The reflectivity change (SEED–NOSEED) in the target region relative to the same change in control regions, i.e. the reflectivity impact parameter (ZIP) and the precipitation impact factor (PIF) as defined in the text. For the WCR, the upwind control is track #1 (with as target tracks #2–#5), and the lateral control is out-of-cone flight section (Fig. 8d) (with as target the in-cone sections, Fig. 8c). For the DOW volume scans, the upwind (lateral) control is the upwind (lateral) control area, and the target in both cases consists of both the upwind and lee target regions (Fig. 10). For the DOW RHI scans, the control is an upwind control only, and the target combines both the upwind and lee target regions (Fig. 13f). (b) The absolute change in reflectivity and derived precipitation rate between SEED and NOSEED in the target region. The horizontal solid line in both panels is the WCR-derived average PBL depth.

First, we examine the temporal change in reflectivity (SEED–NOSEED) in the target regions, which are different for the three different radar systems (Fig. 14b). All three show an increase in reflectivity at low levels, an increase attributed to the strengthening of shallow convection around the time the seeding started. Note that much fewer data exist above 1.5 km AGL since the average cloud depth was around 1.7 km (Fig. 7), therefore average values at higher altitudes are of little significance.

Next, we compare this increase in the target region to any change in the control regions, both upwind and lateral (Fig. 14a). The profiles in Fig. 14a are available only for the DOW and WCR, because there were no echoes during NOSEED in the control MRR profiles. The ZIP values disagree, both for the two radars (DOW and WCR), and for the lateral vs. upwind control, mainly aloft, where fewer data exist. Disagreements can be expected as the measurements periods and regions are different in all four cases, and the sample sizes are relatively small. Unlike for the DOW, WCR data are most common near the ground, so the WCR ZIP/PIF values at low levels (within the boundary layer) are more credible, especially in the lateral control regions. The DOW (lateral control and RHI scans only) and WCR (both lateral and upwind controls) agree that reflectivity increased by 1–5 dB relative to the control region within the boundary layer. The DOW upwind control ZIP profile disagrees with this, but as noted in Section 4.4, this may be a fluke as a convective cell moved through the upwind control region towards the end of SEED.

The low-level relative intensification can be entirely natural: under marginal instability, convection is more likely to initiate over the mountain, as ascent may release potential instability. In other words, an increase in near-surface precipitation rate during seeding in the target region, relative to any trend in the control region, is not conclusive evidence of a positive seeding impact. It can be a natural consequence of orographic convection emerging or intensifying during SEED. But it is less likely that the lateral (along-crest) difference in temporal change of low-level WCR reflectivity is natural as well.

## 5. Seeding impact detection: in situ particle measurements

So far we have focused on radar reflectivity, which is some aggregate measure of the particle size distribution, depending on scattering regime and thus radar wavelength. Now we examine snow size distributions. The basic hypothesis is that the injection of AgI nuclei increases the concentration of ice crystals, although it may decrease the mean ice crystal size (e.g., Super and Boe, 1988).

### 5.1. Flight-level

The UWKA flew at a level of 13 kft MSL, about 660 m above the highest point in the Sierra Madre. The observed convective updrafts and weak winds make it conceivable for AgI nuclei released near the ground and mixed in the boundary layer to impact snow growth over the depth of the orographic cloud, including at flight level. The flight tracks most likely impacted by seeding are tracks #4 and #5 over and just downwind of the Sierra Madre crest (Fig. 1).

The ice crystal concentration is larger in all size bins along these tracks during SEED downwind of the AgI generators (Fig. 15a). Concentrations of snowflakes over  $\sim 1$  mm in diameter (2D-P data) are nearly an order of magnitude larger during SEED. This is consistent with the increase in reflectivity between 0.7 and 1.4 km AGL (the height range of the aircraft AGL along these legs), as shown in Fig. 8b. Also, the flight-level LWC in cloud is very small during NOSEED ( $\sim 0.05 \text{ g m}^{-3}$ ) along tracks #4 and #5, and many sections just contain ice, but during SEED the LWC is much higher in the shallow convective towers, in agreement with ground-based radiometer data (Fig. 3e).

All these changes may be fully consistent with the onset of convection, as stronger updrafts can produce more numerous, larger ice crystals and more liquid water. These changes may have been enhanced by AgI seeding. To examine this, we separate tracks #4 and #5 in two parts, a region downwind of the AgI generators and a lateral control region, identical to the separation of WCR profiles (Fig. 8c–d). The increase in CIP and 2D-P particle concentrations at flight level is much larger downwind of the AgI generators than to the side (Fig. 15). The difference between the two regions is especially significant for small ice crystals (0.1–1 mm diameter). This finding, consistent with that from Fig. 8c–d, is the strongest evidence yet of a seeding impact.

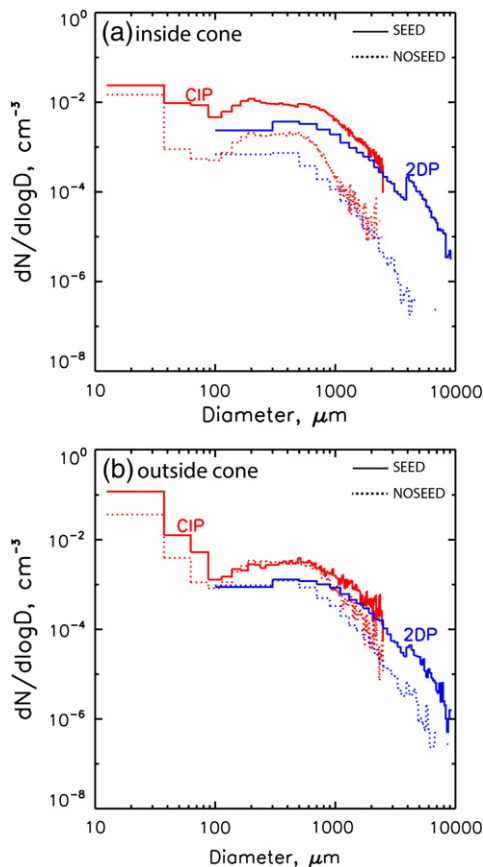


**Fig. 15.** Flight-level particle size distributions from the CIP and the 2D-P optical array probes, averaged for tracks 4 and 5 for the SEED and NOSEED periods (a) inside the cone shown in Fig. 8c (inset) and (b) outside that cone, including the turns between tracks 4 and 5.

## 5.2. Ground-level

The snow trace element analysis (Section 3.4) and wind direction analysis give high confidence that snow falling at Battle Town site was impacted by AgI seeding. Snowfall was quite light at this site during SEED, in fact the heaviest snowfall occurred just after SEED (Fig. 5a), associated with a passing snow shower according to DOW data. We examine snowflake size distributions from a Parsivel disdrometer at Battle Town site (Fig. 16). The NOSEED period is marked by steady, light snowfall with just a few rather large crystals. Snowfall becomes more showery during SEED, consistent with other observations. Snow concentrations dramatically increase during SEED, and mean diameter decreases especially between the showers (Fig. 16b). This could be a seeding impact. It appears rather late and it lingers past the end of the SEED period. This time delay could be due to a longer AgI plume advection time, or to a slow nucleation rate. An increase in snow concentration was observed more than one hour after seeding by Deshler and Reynolds (1990) over the Sierra Nevada.

The Parsivel snow size distribution data is grouped into two parts corresponding with the NOSEED and SEED periods, and then composited as frequency by diameter displays (FDDs) (Fig. 17), with as ordinate the diameter  $D$ , the abscissa the concentration  $N(D)$  (logarithmic scale), and the color fill the normalized count. A nice dipole emerges in the difference FDD (Fig. 17c), with higher concentrations of smaller ice crystals, less than 1 mm diameter during SEED, consistent with flight level measurements (Section 5.1), and consistent with the hypothesis stated at the onset of Section 5. The concentration of larger snowflakes is not substantially impacted.

## 6. Conclusions

This paper presents a detailed case study of a glaciogenically seeded, naturally precipitating orographic cloud sampled on 13 February 2012 during the ASCII experiment over the Sierra Madre range in southern Wyoming. A rich array of instruments was in operation: the profiling airborne W-band WCR, a pair of profiling Ka-band radars (MRRs), and an X-band volume-scanning DOW radar. This paper also analyzes in situ data from a Parsivel disdrometer and several airborne cloud and precipitation probes. An impact of the ground-based AgI seeding on clouds and precipitation is studied by contrasting the measurements from an untreated period (NOSEED) with those from an equally long follow-up period, which was treated (SEED). The design of the project further allows a comparison between control and target regions, which are different for the three radar systems. Fresh snow samples collected near Battle Pass in the target region were analyzed for trace elements to determine whether the snow contained silver from the AgI generators. The key conclusions are as follows:

- > The target storm satisfied basic seeding criteria: there is a high probability that AgI nuclei released from generators along the upwind mountain slope entered a sufficiently cold mixed-phase cloud soon after release.
- > Confidence is high also that snow impacted by AgI seeding fell at Battle Pass, a target site on the mountain,

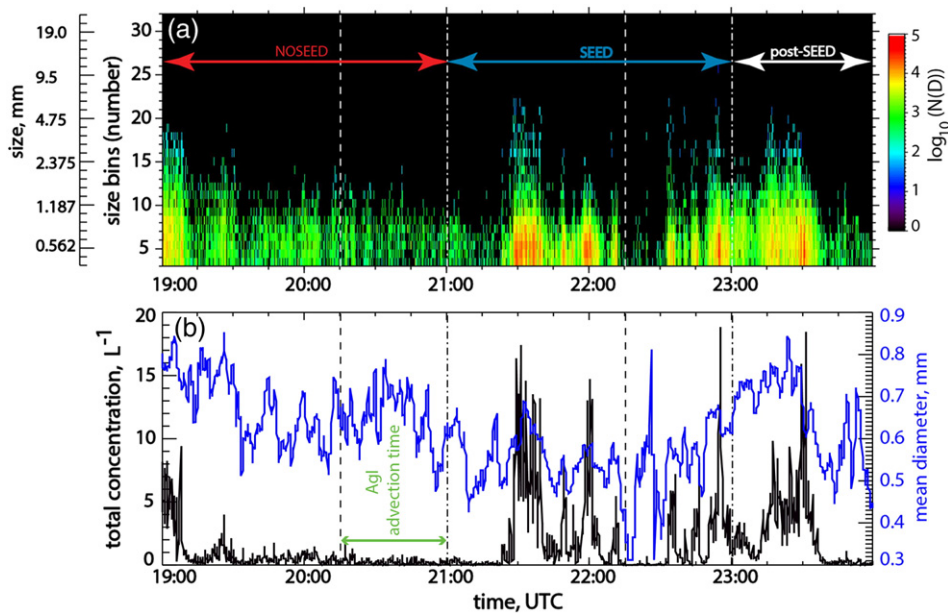


**Fig. 16.** Time series of Parsivel disdrometer measurements at Battle Town site: (a) snow size distribution and (b) total snow concentration (black line) and mean diameter (blue line). The vertical dashed lines in both panels mark the period of AgI generator operation and vertical dash-dot lines indicate an equally long period starting at the estimated arrival time of the AgI plume at Battle Pass.

mainly based on the analysis of trace elements in the snow. There is no independent evidence that cloud and precipitation measured at flight level, some 930 m above Battle Pass, were affected by AgI seeding as well, but it is plausible, given the low wind speed, the well-mixed boundary layer and the presence of convection penetrating to flight level.

- Even though atmospheric conditions were quite steady during the experiment, the lower atmosphere became marginally unstable during the IOP, close to the start of seeding. This resulted in convective clouds, only ~2 km deep from base to top, emerging above a thinning stratiform orographic cloud. These clouds profoundly altered the vertical structure of reflectivity, ice crystal concentrations and size distributions, cloud liquid water and surface snowfall.
- The three radar systems consistently point to an increase in reflectivity at the level where the orographic cumuli emerge during SEED, and down to the lowest detectable level AGL, but this increase tends to occur both over target and control regions. This change at low levels, from NOSEED to SEED, is larger over the target region in the mountains compared with areas to the side of the AgI plumes (lateral control), for the WCR and the DOW, and with the foothills upwind of the AgI generators (upwind control), for the WCR only. This difference and the spatial structure of DOW reflectivity are consistent with orographic convection, growing on the upwind side and collapsing in the lee. The side-by-side trend difference (i.e., target vs. lateral control) for WCR data, which provide the best near-surface coverage, may suggest that seeding enhanced precipitation in the cumuli that emerged across the range, but both the magnitude of the

difference and the sample sizes are too small to firmly make that claim.

- The only evidence for a seeding impact in this case is found not in radar reflectivity data, but rather in ice crystal size distributions, measured at flight level (CIP, 2D-P) and on the ground (Parsivel disdrometer, located near Battle Pass). The ice crystal concentration in all size bins, especially in bins smaller than 1 mm, is significantly larger during SEED both at flight level and at Battle Pass. This too may be a natural consequence of the emergence of shallow convection during SEED, but a comparison between flight sections downwind of the AgI point sources and the “lateral control” sections suggests that glaciogenic seeding significantly increases the concentration of small ice crystals (<1 mm), and may increase the concentration of larger snowflakes as well.

Follow-up work includes a cloud-resolving mountain-scale Large Eddy Simulation of this case, including a parameterization of ice initiation by AgI nuclei released from a point source (Xue et al., 2013).

### Acknowledgments

The ASCII campaign is funded by the National Science Foundation grant AGS-1058426. This work also received funding from the Wyoming Water Development Commission grant 1001552C and the U.S. Geological Survey grant 10000628S, under the auspices of the University of Wyoming Water Research Program. The operation of the AgI generators, the upstream MRR, and the microwave radiometer was supported by the WWMPP, which is funded by the State of Wyoming and managed by Barry Lawrence.

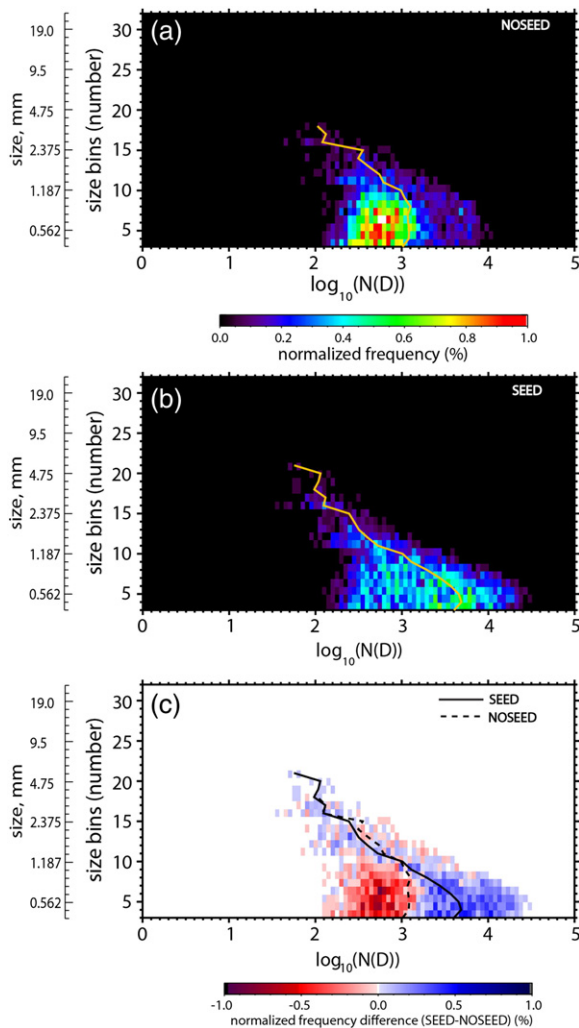


**Fig. 17.** Frequency by diameter display (FDD) of snow particle concentration measured by the Parsivel at Battle Pass during the (a) NOSEED and (b) SEED periods. Panel (c) shows the normalized frequency difference FDD between SEED and NOSEED. The solid yellow lines in (a) and (b) show the average value; these lines are repeated as black lines in (c).

## References

- Austin, P.M., 1987. Relation between measured radar reflectivity and surface rainfall. *Mon. Weather Rev.* 115, 1053–1070.
- Breed, D., Rasmussen, R., Weeks, C., Boe, B., Deshler, T., 2014. Evaluating winter orographic cloud seeding: design of the Wyoming Weather Modification Pilot Project (WWMPP). *J. Appl. Meteorol. Climatol.* 53, 282–299.
- Bruintjes, R.T., 1999. A review of cloud seeding experiments to enhance precipitation and some new prospects. *Bull. Am. Meteorol. Soc.* 80, 805–820.
- Chu, X., Xue, L., Geerts, B., Rasmussen, R., Breed, D., 2014w. A case study of radar observations and WRF LES simulations of the impact of ground-based glaciogenic seeding on orographic clouds and precipitation: part I: observations and model validations. *J. Appl. Meteorol. Climatol.* (in review).
- Creamean, J.M., Suski, K.J., Rosenfeld, D., Cazoria, A., DeMott, P.J., Sullivan, R.C., White, A.B., Ralph, F.M., Minnis, P., Comstock, J.M., Tomlinson, J.M., Prather, K.A., 2013. Dust and biological aerosols from the Sahara and Asian influence precipitation in the Western U.S. *Science* 339, 5172–5177. <http://dx.doi.org/10.1126/science.1227279>.

- DeMott, P.J., 1997. Report to North Dakota atmospheric resource board and weather modification incorporated on tests of the ice nucleating ability of aerosols produced by the Lohse airborne generator. Dept. Atmos. Sci., Colorado State Univ., Report, Fort Collins, CO (15 pp.).
- Deshler, T., Reynolds, D.W., 1990. The persistence of seeding effects in a winter orographic cloud seeded with silver iodide burned in acetone. *J. Appl. Meteorol.* 29, 477–488.
- Elliott, R.D., Shaffer, R.W., Court, A., Hannaford, J.F., 1978. Randomized cloud seeding in the San Juan Mountains, Colorado. *J. Appl. Meteorol.* 17, 1298–1318.
- Gabriel, K.R., 1995. Climax again? *J. Appl. Meteorol.* 34, 1225–1227.
- Garstang, M., Bruintjes, R., Serafin, R., Orville, H., Boe, B., Cotton, W., Warburton, J., 2005. Finding common ground. *Bull. Am. Meteorol. Soc.* 86, 647–655.
- Geerts, B., Miao, Q., Yang, Y., Rasmussen, R., Breed, D., 2010. An airborne profiling radar study of the impact of glaciogenic cloud seeding on snowfall from winter orographic clouds. *J. Atmos. Sci.* 67, 3286–3301.
- Geerts, B., Miao, Q., Yang, Y., 2011. Boundary-layer turbulence and orographic precipitation growth in cold clouds: evidence from profiling airborne radar data. *J. Atmos. Sci.* 68, 2344–2365.
- Geerts, B., Pokharel, B., Friedrich, K., Breed, D., Rasmussen, R., Yang, Y., Miao, Q., Haimov, S., Boe, B., Kalina, E., 2013. The AgI Seeding Cloud Impact Investigation (ASCII) campaign 2012: overview and preliminary results. *J. Weather Modif.* 45, 24–43.
- Gourley, J.J., Tabary, P., Chatelet, J.P.D., 2007. A fuzzy logic algorithm for the separation of precipitating from nonprecipitating echoes using polarimetric radar observations. *J. Atmos. Ocean. Technol.* 24, 1439–1451.
- Grant, L.O., Elliott, R.E., 1974. The cloud seeding temperature window. *J. Appl. Meteorol.* 13, 355–363.
- Hobbs, P.V., Rangno, A.L., 1979. Comments on the climax and Wolf Creek Pass cloud seeding experiments. *J. Appl. Meteorol.* 18, 1233–1237.
- Hobbs, P.V., Lyons, J.H., Locatelli, J.D., Biswas, K.R., Radke, J.F., Weiss, R.R., Rango, A.L., 1981. Radar detection of cloud-seeding effects. *Science* 213, 1250–1252.
- Holroyd, E.W., McPartland, J.T., Super, A.B., 1988. Observation of silver iodide plumes over the Grand Mesa of Colorado. *J. Appl. Meteorol.* 27, 1125–1144.
- Holroyd, E.W., Heimbach, J.A., Super, A.B., 1995. Observations and model simulation of AgI seeding within a winter storm over Utah's Wasatch Plateau. *J. Weather Modif.* 27, 35–56.
- Huggins, A.W., 2007. Another wintertime cloud seeding case study with strong evidence of seeding effects. *J. Weather Modif.* 39, 9–36.
- Kirschbaum, D.J., Durran, D.R., 2004. Factors governing cellular convection in orographic precipitation. *J. Atmos. Sci.* 61, 682–698.
- Korolev, A.V., Emery, E.F., Strapp, J.W., Cober, S.G., Isaac, G.A., 2013. Quantification of the effects of shattering on airborne ice particle measurements. *J. Atmos. Ocean. Technol.* 30, 2527–2553.
- Kristovich, D.A.R., Geerts, B., Miao, Q., Stoecker, L., Ritzman, J.M., 2012. Airborne cloud radar and lidar observations of blowing snow during the ASCII project: a possible natural cloud seeding mechanism. *Proc. AMS 19th Conf. on Mountain Meteorology. Amer. Meteor. Soc., Steamboat Springs, CO* (Available online at <https://ams.confex.com/ams/15MountMet/webprogram/Paper210260.html>).
- Maahn, M., Kollias, P., 2012. Improved Micro Rain Radar snow measurements using Doppler spectra post-processing. *Atmos. Meas. Tech.* 5, 2661–2673.
- Manton, M.J., Warren, L., 2011. A confirmatory snowfall enhancement project in the Snowy Mountains of Australia. Part II: primary and associated analyses. *J. Appl. Meteorol. Climatol.* 50, 1448–1458.
- Markowski, P., Richardson, Y., 2010. *Mesoscale Meteorology in Midlatitudes*. Wiley-Blackwell, (407 pp.).
- Matrosov, S.Y., 2007. Modeling backscatter properties of snowfall at millimeter wavelengths. *J. Atmos. Sci.* 64, 1727–1736.
- Mielke, P.W., Grant, L.O., Chappell, C.F., 1970. Elevation and spatial variation effects of wintertime orographic cloud seeding. *J. Appl. Meteorol.* 9, 476–488.
- Mielke, P.W., Brier, G.W., Grant, L.O., Mulvey, G.J., Rosenzweig, P.N., 1981. A statistical reanalysis of the replicated Climax I and II Wintertime orographic cloud seeding experiments. *J. Appl. Meteorol.* 20, 643–659.
- National Research Council, 2003. *Critical Issues in Weather Modification Research*. National Academy Press, (123 pp.).
- Oye, R., Mueller, C., Smith, S., 1995. Software for radar translation, visualization, editing, and interpolation. Preprints, 27th Conf. on Radar Meteorology. Amer. Meteor. Soc., Vail, CO, pp. 359–361.
- Plummer, D., McFarquhar, G.M., Rauber, R.M., Leon, D., 2014w. Structure and statistical analysis of the microphysical properties of generating cells in the comma-head region of continental winter cyclones. *J. Atmos. Sci.* (in review).
- Pokharel, B., Geerts, B., 2014. The impact of glaciogenic seeding on snowfall from shallow orographic clouds over the Medicine Bow Mountains in Wyoming. *J. Weather Modif.* (accepted for publication).
- Pokharel, B., Vali, G., 2011. Evaluation of collocated measurements of radar reflectivity and particle sizes in ice clouds. *J. Appl. Meteorol. Climatol.* 50, 2104–2119.

- Pokharel, B., Geerts, B., Jing, X., 2014. The impact of ground-based glaciogenic seeding on orographic clouds and precipitation: a multi-sensor case study. *J. Appl. Meteorol. Climatol.* 53, 890–909.
- Rasmussen, R., Dixon, M., Vasiloff, S., Hage, F., Knight, S., Vivekanandan, J., Xu, M., 2003. Snow nowcasting using a real-time correlation of radar reflectivity with snow gauge accumulation. *J. Appl. Meteorol.* 42, 20–36.
- Rogers, D.C., Vali, G., 1987. Ice crystal production by mountain surfaces. *J. Clim. Appl. Meteorol.* 26, 1152–1168.
- Rosenow, A., Plummer, D., Rauber, R., McFarquhar, G., Jewett, B., Leon, D., 2014. Vertical velocity and physical structure of generating cells and convection in the comma head region of continental winter cyclones. *J. Atmos. Sci.* 71, 1538–1658.
- Seto, J., Tomine, K., Wakimizu, K., Nishiyama, K., 2011. Artificial cloud seeding using liquid carbon dioxide: comparisons of experimental data and numerical analysis. *J. Appl. Meteorol. Climatol.* 50, 1417–1431.
- Super, A.B., 1999. Summary of the NOAA/Utah atmospheric modification program: 1990–1998. *J. Weather Modif.* 31, 51–75.
- Super, A.B., Boe, B.A., 1988. Microphysical effects of wintertime cloud seeding with silver iodide over the Rocky Mountains. Part III: observations over the Grand Mesa, Colorado. *J. Appl. Meteorol.* 27, 1166–1182.
- Super, A.B., Heimbach, J.A., 1988. Microphysical effects of wintertime cloud seeding with silver iodide over the Rocky Mountains. Part II: observations over the Bridger Range, Montana. *J. Appl. Meteorol.* 27, 1152–1165.
- Vardiman, L., Moore, J.A., 1978. Generalized criteria for seeding winter orographic clouds. *J. Appl. Meteorol.* 17, 1769–1777.
- Vonnegut, B., 1947. The nucleation of ice formation by silver iodide. *J. Appl. Phys.* 18, 593–595.
- Wang, Z., French, J., Vali, G., Wechsler, P., Haimov, S., Rodi, A., Deng, M., Leon, D., Snider, J., Peng, L., Pazmany, A.L., 2012. Single aircraft integration of remote sensing and in situ sampling for the study of cloud microphysics and dynamics. *Bull. Am. Meteorol. Soc.* 93, 653–668.
- Wiacek, A., Peter, T., Lohmann, U., 2010. The potential influence of Asian and African mineral dust on ice, mixed-phase and liquid water clouds. *Atmos. Chem. Phys.* 10, 8649–8667.
- World Meteorological Organization (WMO), 2010. Executive summary of the WMO statement on weather modification. Meeting of the Expert Team on Weather Modification Research, Abu Dhabi, United Arab Emirates (13 pp.).
- Xue, L., Tessendorf, S., Nelson, E., Rasmussen, R., Breed, D., Parkinson, S., Holbrook, P., Blestrud, D., 2013. Implementation of a silver iodide cloud seeding parameterization in WRF. Part II: 3D simulations of actual seeding events and sensitivity tests. *J. Appl. Meteorol. Climatol.* 52, 1458–1476.
- Yuter, S., Houze, R.A., 1995. Three-dimensional kinematic and microphysical evolution of Florida cumulonimbus. Part II: frequency distributions of vertical velocity, reflectivity, and differential reflectivity. *Mon. Weather Rev.* 123, 1941–1963.
- Yuter, S.E., Kingsmill, D.E., Nance, L.B., Löffler-Mang, M., 2006. Observations of precipitation size and fall speed characteristics within coexisting rain and wet snow. *J. Clim. Appl. Meteorol.* 45, 1450–1464.